Flow of viscoelastic jet with moderate inertia near channel exit

AMIR SAFFARI AND ROGER E. KHAYAT†

Department of Mechanical and Materials Engineering, The University of Western Ontario, London, Ontario, Canada N6A 5B9

The steady-state moderately inertial jet flow of a viscoelastic liquid of the Oldroyd-B type, emerging from a two-dimensional channel, is examined theoretically in this study. Poiseuille flow conditions are assumed to prevail far upstream from the exit. The problem is solved using the method of matched asymptotic expansions. The small parameter involved in the expansions is the inverse Reynolds number. The flow and stress fields are obtained as composite expansions by matching the flow in the boundary-layer region near the free surface and the flow in the core region. The influence of elasticity on the shape of the free surface, the profiles of velocity and stress and the interplay between inertia and elasticity are explored. It is found that even for a jet with moderate inertia, elastic effects play a significant role, especially close to the channel exit near the free surface. It is also found that similar to the Newtonian case, the viscoelastic jet contracts downstream from the channel exit. However, in contrast to Newtonian jet, a viscoelastic jet is preceded by a flat region very close to the channel exit at which elastic and inertial effects are in balance. The extent of this region increases with elasticity. A momentum integral balance is applied to validate the theory and obtain the jet contraction ratio explicitly in terms of the Deborah number, viscosity ratio and Reynolds number.

1. Introduction

The interplay between inertia and elasticity is examined in this study for the two-dimensional steady flow of an incompressible viscoelastic fluid exiting a channel (see figure 1). The emphasis is on the flow near exit. Inertia is assumed to remain relatively important, allowing asymptotic development in terms of the inverse Reynolds number. Similar to Newtonian jet (Tillett 1968), the flow is supposed to have the basic Poiseuille profile to lowest order and is modified when the fluid leaves the channel in the form of a jet. When the fluid detaches itself from the wall of the channel, the removal of the wall stress causes a boundary layer to form in a region near the free surface; in this region the parabolic velocity profile adjusts itself so as to satisfy the condition of zero traction at the free surface. In the case of an inviscid liquid, this condition would not be imposed, and all the conditions of the problem would be satisfied by postulating that the parabolic profile continues unchanged in the jet region. However, no uniqueness theorem exists for this inviscid problem, and it is conceivable that other solutions might exist; nevertheless, it is assumed in this paper that Poiseuille flow everywhere is the proper inviscid limit (see Tillett 1968). With this assumption,

† Email address for correspondence: rkhayat@uwo.ca

the flow in the core of the jet is, to lowest order, not affected by the flow in the boundary-layer region near the free surface, although the boundary layer is expected to induce perturbations to the basic Poiseuille flow, when higher-order terms are included, for the flow both upstream and downstream from the channel exit.

Liquid laminar jets have been extensively studied previously in the literature. However, the focus has mainly been on Newtonian jet flow. In addition, in most studies of Newtonian jets, due to the convective nonlinearities, limited studies can be found, which take inertial effect into account. For high-inertial jet flow of Newtonian fluids, Tillett (1968) used the method of matched asymptotic expansions for a planar steady jet. He developed a classical boundary-layer analysis to find the flow at small distances downstream of the jet. Similar to all boundary-layer analyses, where the solution is not valid within a small distance from inception such as very near the leading edge and stagnation point, Tillett's analysis precludes the flow at the channel exit. However, the distance in question is small, of the order of the (local) boundary-layer thickness. Consequently, the boundary-layer approach turns out to be successful in capturing the flow nature near inception. Miyake, Mukai & Iemoto (1979) carried out an analysis similar to Tillett's on a vertical jet of inviscid fluid taking into account gravity effect. Philippe & Dumargue (1991) also applied an analysis similar to Tillett's for viscous axisymmetric vertical jets, emphasizing the interplay between gravity and inertia effects on the free-surface shape and the velocity profile. A local similarity transformation was carried out by Wilson (1985) for the axisymmetric viscous-gravity jet for the boundary-layer-type flow close to the free surface.

Generally, non-Newtonian jets are more likely to remain laminar compared to Newtonian jets (Rotem 1964; Cao *et al.* 2005; German & Khayat 2008). This makes the assumption of laminar flow within a distance downstream more plausible. The axisymmetric free laminar jet of an incompressible pseudoplastic fluid was investigated by Rotem (1964). A boundary-layer approximation was used to find the velocity profiles for different exponents in an inelastic fluid. Submerged planar and axisymmetric jet flows of non-Newtonian power-law fluids at high Reynolds number have been investigated by Stehr & Schneider (2000). They used the method of matched asymptotic expansions and accounted for interaction between the jet flow and the induced flow.

Regarding the jet flow of viscoelastic fluids, the focus has mainly been in the literature on die swell. For instance Tieu & Joseph (1983) considered surface-tension-driven flow, and Tran-Cong & Phan-Thien (1988) examined the creeping-flow extrusion of a viscoelastic fluid from triangular and square dies. Of closer relevance to the present problem, Liang, Oztekin & Neti (1999) carried out flow visualization and measurement to describe the behaviour of steady viscoelastic jet issuing from a capillary or an orifice under gravity. Their experiments revealed that depending upon the elasticity level of the fluid, the jet width may increase, decrease or remain unchanged downstream from the exit at least within a certain distance from the exit. In this case, the interplay between gravity and elasticity dictates the jet behaviour. Interestingly, one may expect similar or parallel observations upon examining the interplay between inertia and elasticity as in the current study. Indeed, both gravity and inertia tend to have a stabilizing effect (Cao, Khayat & Puskas 2005). Finally, the breakup of viscoelastic jets has been theoretically analysed by Goldin *et al.* (1969), Shummer & Thelen (1988) and Renardy (2002).

The numerical computation of viscoelastic fluid flows with differential constitutive equations presents various difficulties, especially for free-surface flow. These difficulties are usually due to the lack of convergence and stability of the complex numerical

scheme handling nonlinearities of inertial, elastic and geometrical nature. In addition, due to the hybrid type of the governing equations (elliptic and hyperbolic), geometrical singularities such as re-entrant corner or die induce stress singularities and hence numerical problems. Bérdaudo *et al.* (1998) examined the die-swell phenomenon preceded by a confined convergent two-dimensional and axisymmetric geometries for a viscoelastic fluid using the finite-element method. In their study, they neglected inertia but claimed that it could be included without any difficulty. Therein, a summary of computational studies on viscoelastic flows and the associated complexities can be found.

The present study is restricted to flows with inertia dominating elastic and viscous effects. The work is of fundamental importance given the significant qualitative role that elasticity plays in this case. In general, inertia has been neglected in most of the studies on viscoelastic jets. This can be quite reasonably justified, since in most practical applications of polymeric liquids, inertia is effectively small. However, there are still applications such as fibre spinning (Donnelly & Weinberger 1975), film casting (Cao *et al.* 2005) and high-speed extrusions (Slattery & Lee 2000) in which inertia plays a significant role. Shah & Pearson (1972) showed that inertia plays a very important role in fibre spinning, as it enhances flow stability. Inertia becomes particularly important in modern high-speed film casting (Cao *et al.* 2005). Experiments on film casting and fibre spinning (Doufas & McHugh 2001; Seyfzadeh, Harrison & Carlson 2005) also suggest that inertia has a significant effect on the stability region of these processes. In a recent study by German & Khayat (2008), the effects of inertia and elasticity were examined for the film casting of a Phan–Thien–Tanner fluid. Linear stability analysis was carried out. It was shown that inertia has a stabilizing effect on the film-casting flow. The reader is referred to German & Khayat (2008) for further discussion.

Middleman & Gavis (1961) observed in their experiments that the viscoelastic jet expands for low ejection velocities. The expansion reaches a maximum with increasing flow rate. However, the expansion begins to weaken as the flow rate is increased further, and the viscoelastic jet ultimately contracts when inertia becomes significant. In their study, however, they used only a power-law model to represent the fluid properties, which does not allow a direct quantitative comparison with the results of the present study. A similar interplay between inertia and elasticity is also responsible for the delayed die-swell phenomenon. Delayed swell appears to be caused by some inertial mechanism related to the change in flow type from subcritical to supercritical (Cloitre *et al.* 1998). More recently, Khayat & Kim (2006) examined the flow of a viscoelastic thin jet emerging from an annulus. In this case, a boundary-layer approach was used to approximate the flow throughout the jet thickness. Such an approach cannot be used for the present problem, as no restriction is placed on its thickness. The interplay between inertia and elasticity was also considered in other flows of some relevance to the present study. Eggleton, Ferziger & Pulliam (1994) examined the steady-state entry flow of an Oldroyd-B fluid in a planar channel using perturbation analysis. They predicted entrance lengths shorter than those of a Newtonian fluid at moderate Reynolds numbers.

In the present study, the role of elasticity in a moderately inertial jet flow and the interplay between inertia and elasticity are investigated. The formulation and solution procedure follow those of Tillett (1968). However, the solution is now found for the boundary-layer-type equations derived for a viscoelastic Oldroyd-B fluid (Oldroyd 1950; Bird, Armstrong & Hassager 1987). The solution is developed in powers of ε, where ε^3 is the inverse Reynolds number, both in the 'inner' boundary-layer region

and in the 'outer' core region. The two expansions are matched by the standard procedure suggested by Van Dyke (1964). Special emphasis is placed on the effect of elasticity of the liquid on the shape of the free surface and the profiles of the velocity and stress components close to the exit. Good qualitative agreement is found with the measurements and observations of Liang *et al.* (1999). The results are most likely to be useful as reference for comparison with future experiment and numerical simulation. Finally, and very importantly, in typical jet flow calculations, Poiseuille conditions are assumed at inception. The present work provides the correct conditions near exit, which are required to determine the jet structure further downstream.

2. Governing equations

The fluid is assumed to be an incompressible polymeric solution of density ρ, relaxation time λ and viscosity μ. In this study, only fluids that can be reasonably represented by a single relaxation time and constant viscosity are considered. The polymeric solution is assumed to be composed of a Newtonian solvent of viscosity μ_s and a polymeric solute of viscosity μ_p, such that the solution viscosity is given by $\mu = \mu_s + \mu_p$. Regardless of the nature of the fluid, the continuity and momentum balance equations must hold. The conservation equations for an incompressible fluid can be concisely written as

$$\nabla \cdot U = 0, \tag{2.1}$$

$$\rho(U_T + U \cdot \nabla U) = -\nabla P + \nabla \cdot \Sigma, \tag{2.2}$$

where U is the velocity vector; P is the pressure; T is the time; and ∇ is the gradient operator. A subscript denotes partial differentiation. The stress tensor Σ comprises a Newtonian component, corresponding to the Newtonian solvent, and a polymeric component T corresponding to the solute. Thus,

$$\Sigma = \mu_s(\nabla U + \nabla U^t) + T, \tag{2.3}$$

where t denotes matrix transposition. The constitutive equation for T is taken to correspond to the Oldroyd-B fluid, which can be written as (Bird *et al.* 1987)

$$\lambda(T_T + U \cdot \nabla T - T \cdot \nabla U - \nabla U^t \cdot T) + T = \mu_p(\nabla U + \nabla U^t). \tag{2.4}$$

In the limit $\mu_s \to 0$, system (2.1)–(2.4) reduces to that corresponding to a Maxwell fluid. In the limit $\mu_p \to 0$, the Navier–Stokes equations are recovered. The problem is now examined in a Cartesian coordinate system using standard notations for velocity and stress components.

Consider the flow of a viscoelastic jet emerging from a channel as schematically depicted in figure 1 in the (X, Z)-plane. The X-axis is taken along the lower edge of the channel, and the Z-axis is chosen in the transverse direction across the channel. The channel exit coincides with $X = 0$. The flow is induced by a pressure gradient inside the channel. It is convenient to introduce the stress components as $Q \equiv T_{xx}$, $R \equiv T_{zz}$ and $S \equiv T_{xz} = T_{zx}$. The stream function and corresponding stress components of the basic Poiseuille flow are given by

$$\Psi = A\left(Z^2 - \frac{2}{3b}Z^3\right), \tag{2.5a}$$

$$Q = 4\lambda A S\left(1 - \frac{2Z}{b}\right) = 8\lambda \mu_p A^2 \left(1 - \frac{2Z}{b}\right)^2, \tag{2.5b}$$
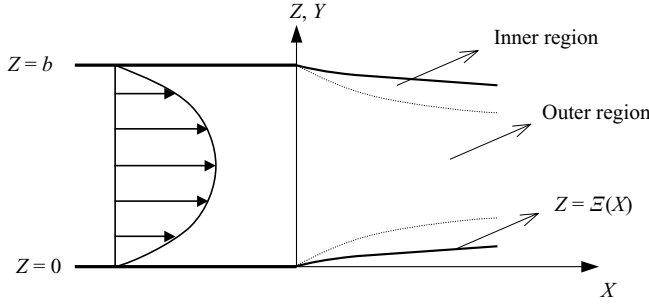
FIGURE 1. Schematic illustration of the planar jet flow, including the upstream and downstream regions from the channel exit, as well as the free surfaces. All notations are dimensional.

$$R = 0, \tag{2.5c}$$

$$S = 2\mu_p A \left(1 - \frac{2Z}{b} \right), \tag{2.5d}$$

where b is the width of the channel and $A = 3\bar{U}/b$, with $\bar{U}$ being the average velocity in the channel. Following Tillett (1968), a Reynolds number Re based on the channel width is introduced. For a viscoelastic fluid, there are two additional non-dimensional similarity parameters, namely the solvent-to-solute viscosity ratio Rv and the Deborah number De. Explicitly written, these parameters take the following form:

$$Re = \frac{Ab^2}{\nu}, \quad Rv = \frac{\mu_s}{\mu_p}, \quad De = \lambda A, \tag{2.6}$$

where ν is the kinematic viscosity. The solute-to-solution viscosity ratio is introduced as $a = 1/(1 + Rv)$. In this problem, $1/Re$ is assumed to be the small, and both Rv and De are assumed to be of order one. The Deborah number in (2.6) is introduced in terms of shear rate and is more commonly referred to as the Weissenberg number in the literature. A variable Y is conveniently introduced to denote the deviation from the free surface, namely

$$Y = Z - \varXi(X, Re, De, Rv), \tag{2.7}$$

where $Z = \varXi(X, Re, De, Rv)$ is the equation of the lower free surface. Non-dimensional variables are introduced by measuring lengths with respect to b, stream function with respect to Ab^2, pressure with respect to $\rho A^2 b^2$ and polymeric stress components with respect to μA and are given by

$$\left. \begin{aligned} X = bx, \quad Z = bz, \quad \varXi = b\zeta, \\ P = \rho A^2 b^2 p, \quad \varPsi = Ab^2 \psi, \quad (Q, S, R) = \mu A(q, s, r). \end{aligned} \right\} \tag{2.8}$$

Now, (2.5a)–(2.5d) become

$$\psi_0 = z^2 - \frac{2}{3}z^3, \tag{2.9a}$$

$$r_0 = 0, \tag{2.9b}$$

$$s_0 = a\psi_{0zz} = 2a(1 - 2z), \tag{2.9c}$$

$$q_0 = 2De\, s_0 \psi_{0zz} = 8a\, De(1 - 2z)^2, \tag{2.9d}$$

and accordingly, the non-dimensional conservation of momentum and constitutive equations for the laminar steady flow take the following form:

$$\psi_z \psi_{xz} - \psi_x \psi_{zz} = -p_x + \frac{aRv}{Re}(\psi_{xxz} + \psi_{zzz}) + \frac{1}{Re}(q_x + s_z), \tag{2.10a}$$

$$-\psi_z \psi_{xx} + \psi_x \psi_{xz} = -p_z - \frac{aRv}{Re}(\psi_{xxx} + \psi_{xzz}) + \frac{1}{Re}(s_x + r_z), \tag{2.10b}$$

$$De(\psi_z q_x - \psi_x q_z - 2q\psi_{xz} - 2s\psi_{zz}) + q = 2a\psi_{xz}, \tag{2.11a}$$

$$De(\psi_z r_x - \psi_x r_z + 2s\psi_{xx} + 2r\psi_{xz}) + r = -2a\psi_{xz}, \tag{2.11b}$$

$$De(\psi_z s_x - \psi_x s_z + q\psi_{xx} - r\psi_{zz}) + s = a(\psi_{zz} - \psi_{xx}). \tag{2.11c}$$

For $x > 0$ the kinematic and dynamic boundary conditions at the free surface, $z = \zeta(x)$, are

$$\psi = 0, \tag{2.12a}$$

$$p + \frac{1}{Re}[aRv(2\psi_{xz} + \zeta'\psi_{zz} - \zeta'\psi_{xx}) + \zeta's - r] = 0, \tag{2.12b}$$

$$p\zeta' - \frac{1}{Re}[aRv(2\psi_{xz}\zeta' - \psi_{zz} + \psi_{xx}) + q\zeta' - s] = 0. \tag{2.12c}$$

A prime denotes total differentiation. Note that surface tension effect is assumed to be negligible. Philippe & Dumargue (1991) showed that even in the case of a high-Reynolds-number cylindrical Newtonian jet with two radii of curvature, surface tension effect is negligible for most ordinary liquids. Surface tension is expected to be even less significant for polymeric liquids (see Khayat & Kim 2006).

Given the symmetry of the flow, the problem is examined over the range $0 \leqslant z \leqslant 1/2$; the flow for $1/2 \leqslant z \leqslant 1$ can be obtained similarly. Inside the channel, the following conditions must be satisfied:

$$\psi = \frac{1}{6} \quad \text{at } z = \frac{1}{2}, \tag{2.13a}$$

$$\psi_z = 0 \quad \text{at } z = 0, \tag{2.13b}$$

$$\psi \to z^2 - \frac{2}{3}z^3 \quad \text{at } x \to -\infty, \tag{2.13c}$$

$$r \to 0, \; s \to 2a(1 - 2z), \; q \to 8aDe(1 - 2z)^2 \quad \text{as } x \to -\infty. \tag{2.13d}$$

The problem is now examined by considering separately the flow near the free surface (inner region) and the flow in the core (outer) region. The composite flow is obtained upon matching the solutions at the interface between the two regions (see figure 1).

3. The inner expansion

To examine the boundary-layer structure near the free surface, the scaling in the transverse direction is changed by writing $y = \varepsilon\eta$, where $\varepsilon = Re^{-\alpha}$ and α is to be determined. Anticipating that the height ζ of the free surface is of the same order of magnitude as the boundary-layer thickness, one can write $\zeta(x) = \varepsilon h(x)$ and henceforth work with h. It is not necessary to assume that $h(x) = O(1)$ as $\varepsilon \to 0$; examination of (3.2a) shows that the inner expansion developed in this section holds provided only that $h = o(\varepsilon^{-1})$, i.e. ζ tends to 0 with ε. In the matching process, in §5, it will be

shown that $h = O(1)$. Making the change of independent variables

$$\begin{cases} x = \xi, \\ z = \varepsilon(\eta + h), \end{cases} \tag{3.1}$$

in (2.10a) and (2.10b), it is concluded that

$$\psi_\eta \psi_{\xi\eta} - \psi_\xi \psi_{\eta\eta} = -\varepsilon^2(p_\xi - h'p_\eta) + aRv\varepsilon^{\left(\frac{1}{\alpha}-1\right)}\psi_{\eta\eta\eta} + aRv\varepsilon^{\left(\frac{1}{\alpha}+1\right)}$$

$$\times \left(\psi_{\xi\xi\eta} - h''\psi_{\eta\eta} - 2h'\psi_{\xi\eta\eta} + h'^2\psi_{\eta\eta\eta} + \frac{1}{aRv}s_\eta\right) + \varepsilon^{2+\frac{1}{\alpha}}(q_\xi - h'q_\eta), \quad (3.2a)$$

$$-\psi_\eta \psi_{\xi\xi} + \psi_\xi \psi_{\xi\eta} + h''\psi_\eta^2 + h'(\psi_\eta \psi_{\xi\eta} - \psi_\xi \psi_{\eta\eta}) = -p_\eta + \varepsilon^{\frac{1}{\alpha}}r_\eta - aRv\varepsilon^{\left(\frac{1}{\alpha}-1\right)}$$

$$\times (\psi_{\xi\eta\eta} - h'\psi_{\eta\eta\eta}) - aRv\varepsilon^{\left(\frac{1}{\alpha}+1\right)}\left[\left(\frac{\partial}{\partial\xi} - h'\frac{\partial}{\partial\eta}\right)^3 \psi - \frac{1}{aRv}(s_\xi - h's_\eta)\right]. \quad (3.2b)$$

Note that ξ and x are distinguished only in differentiation.

The aim is to find a solution of these equations in the form of an 'inner expansion' in ε. In order to match this to the outer Poiseuille flow, it is necessary to have $\psi \sim y^2$ as $\eta \to \infty$ in the inner region, to lowest order in ε; so ψ must be of order ε^2. In order to determine the value of α, it is required to find the order of the polymeric stress components in (3.2a) and (3.2b) first. The constitutive equations for the polymeric stress components, (2.11a)–(2.11c), can be written explicitly in terms of inner variables as

$$De(\varepsilon uq_\xi - \varepsilon h'uq_\eta + wq_\eta - 2\varepsilon qu_\xi + 2\varepsilon h'qu_\eta - 2ru_\eta) + \varepsilon q = 2a\varepsilon(u_\xi - h'u_\eta), \quad (3.3a)$$

$$De(\varepsilon ur_\xi - \varepsilon h'ur_\eta + wr_\eta - 2\varepsilon sw_\xi + 2\varepsilon h'sw_\eta - 2rw_\eta) + \varepsilon r = 2a(w_\eta), \quad (3.3b)$$

$$De(\varepsilon us_\xi - \varepsilon h'us_\eta + ws_\eta - \varepsilon qw_\xi + \varepsilon h'qw_\eta - ru_\eta) + \varepsilon s = a(u_\eta + \varepsilon w_\xi - \varepsilon h'w_\eta), \quad (3.3c)$$

where the components u, the streamwise velocity, and w, the transverse velocity, are now expressed in terms of the stream function as

$$u = \psi_z = \frac{1}{\varepsilon}\psi_\eta, \tag{3.4a}$$

$$w = -\psi_x = -\psi_\xi + h'\psi_\eta. \tag{3.4b}$$

From (3.4a), it is obvious that u is of order ε. Considering the fact that u in the inner region must match the velocity in the outer region, $u = \psi_z = 2z - 2z^2$, it is also inferred that u must be of order ε inside the inner region. The order of w can be found using the continuity equation when written in terms of inner variables, or

$$\varepsilon u_\xi - \varepsilon h'u_\eta + w_\eta = 0. \tag{3.5}$$

Thus, w is of order ε^2.

Now that the order of magnitudes of velocity components has been determined, it can be simply deduced from (3.3a)–(3.3c) that q and s are of order one whereas r is of order ε, in the inner region. It is not difficult to realize that both s and q are of order one, since they need to match the stresses in the outer region. However, the order of r is determined by inspecting (3.3b); it will be shown that r vanishes in the outer region. In this case, a balance among the viscous, inertial and polymeric stress terms in (3.2a) and (3.2b) is achieved upon taking $\alpha = 1/3$. In this case, the momentum conservation equations can be rewritten as

$$\psi_\eta \psi_{\xi\eta} - \psi_\xi \psi_{\eta\eta} = -\varepsilon^2(p_\xi - h'p_\eta) + aRv\varepsilon^2 \psi_{\eta\eta\eta} + aRv\varepsilon^4$$
$$\times \left(\psi_{\xi\xi\eta} - h''\psi_{\eta\eta} - 2h'\psi_{\xi\eta\eta} + h'^2\psi_{\eta\eta\eta} + \frac{1}{aRv}s_\eta \right) + \varepsilon^5(q_\xi - h'q_\eta), \quad (3.6a)$$

$$-\psi_\eta \psi_{\xi\xi} + \psi_\xi \psi_{\xi\eta} + h''\psi_\eta^2 + h'(\psi_\eta \psi_{\xi\eta} - \psi_\xi \psi_{\eta\eta}) = -p_\eta + \varepsilon^3 r_\eta - aRv\varepsilon^2$$
$$\times (\psi_{\xi\eta\eta} - h'\psi_{\eta\eta\eta}) - aRv\varepsilon^4 \left[\left(\frac{\partial}{\partial\xi} - h'\frac{\partial}{\partial\eta} \right)^3 \psi - \frac{1}{aRv}(s_\xi - h's_\eta) \right]. \quad (3.6b)$$

The boundary conditions on the free surface $\eta = 0$ are, from (2.12a)–(2.12c),

$$\psi = 0, \qquad (3.7a)$$

$$\varepsilon(h'p + aRv\,\psi_{\eta\eta}) - \varepsilon^3 aRv \left[\left(\frac{\partial}{\partial\xi} - h'\frac{\partial}{\partial\eta} \right)^2 \psi + 2h'(\psi_{\xi\eta} - h'\psi_{\eta\eta}) \right] + \varepsilon^4 h'q + \varepsilon^3 s = 0,$$
$$(3.7b)$$

$$p + \varepsilon^2 aRv[2\psi_{\xi\eta} - h'\psi_{\eta\eta}] - \varepsilon^4 h'aRv \left(\frac{\partial}{\partial\xi} - h'\frac{\partial}{\partial\eta} \right)^2 \psi + \varepsilon^4 h's - \varepsilon^3 r = 0. \quad (3.7c)$$

The inner expansion for ψ begins with a term in ε^2. This is assumed until there is evidence to the contrary. Thus, the expansion proceeds in powers of ε, so that

$$\psi(\xi, \eta) = \varepsilon^2 \Psi_2(\xi, \eta) + \varepsilon^3 \Psi_3(\xi, \eta) + \dots. \qquad (3.8)$$

Similarly, h and p are expanded as

$$h(\xi) = \varepsilon^{-1}\zeta(\xi) = h_0(\xi) + \varepsilon h_1(\xi) + \dots, \qquad (3.9)$$
$$p(\xi, \eta) = P_0(\xi, \eta) + \varepsilon P_1(\xi, \eta) + \dots. \qquad (3.10)$$

From (3.6b), (3.7c) and (3.10), it can be concluded that p is of order ε^4. In order to solve (3.6a), it is required to express the stress components in terms of the stream function. This can be done by expanding each of the velocity and stress components as regular expansions as follows:

$$u(\xi, \eta) = \varepsilon U_1(\xi, \eta) + \varepsilon^2 U_2(\xi, \eta) + \dots, \qquad (3.11a)$$
$$w(\xi, \eta) = \varepsilon^2 W_2(\xi, \eta) + \varepsilon^3 W_3(\xi, \eta) + \dots, \qquad (3.11b)$$
$$q(\xi, \eta) = Q_0(\xi, \eta) + \varepsilon Q_1(\xi, \eta) + \dots, \qquad (3.11c)$$
$$s(\xi, \eta) = S_0(\xi, \eta) + \varepsilon S_1(\xi, \eta) + \dots, \qquad (3.11d)$$
$$r(\xi, \eta) = \varepsilon R_1(\xi, \eta) + \varepsilon^2 R_2(\xi, \eta) + \dots. \qquad (3.11e)$$

In this case, $U_1 = \Psi_{2\eta}$, $U_2 = \Psi_{3\eta}$, $W_2 = -\Psi_{2\xi} + h_0'\Psi_{2\eta}$ and so on. Hence, the stress components can be expressed to any order in terms of stream functions of different orders. Thus, upon using (3.8), (3.9) and (3.11), (3.3) gives, to $O(\varepsilon)$,

$$Q_0 = 2aDe\Psi_{2\eta\eta}^2, \qquad (3.12a)$$
$$R_0 = 0, \qquad (3.12b)$$
$$S_0 = a\Psi_{2\eta\eta}, \qquad (3.12c)$$
$$Q_1 = 2a(\Psi_{2\xi\eta} - h_0'\Psi_{2\eta\eta}) - aDe[6De\Psi_{2\eta\eta}\Psi_{2\eta\eta\xi}\Psi_{2\eta} \qquad (3.12d)$$
$$\qquad - 6De\Psi_{2\eta\eta}\Psi_{2\eta\eta\eta}\Psi_{2\xi} - 4\Psi_{2\eta\eta}\Psi_{3\eta\eta}],$$
$$R_1 = 2a(-\Psi_{2\xi\eta} + h_0'\Psi_{2\eta\eta}), \qquad (3.12e)$$
$$S_1 = a\Psi_{3\eta\eta} - aDe\left(\Psi_{2\eta}\Psi_{2\xi\eta\eta} - \Psi_{2\xi}\Psi_{2\eta\eta\eta} + 2\Psi_{2\xi\eta}\Psi_{2\eta\eta} - 2h_0'\Psi_{2\eta\eta}^2 \right). \qquad (3.12f)$$

Using (3.12), the momentum equation, (3.6a), to leading order, reads

$$\Psi_{2\eta}\Psi_{2\xi\eta} - \Psi_{2\xi}\Psi_{2\eta\eta} = \Psi_{2\eta\eta\eta}. \tag{3.13}$$

Note that (3.6b) is not immediately needed because of the decoupling of the pressure. The corresponding boundary conditions are obtained from (3.7a) and (3.7b), namely

$$\Psi_2(\xi, 0) = \Psi_{2\eta\eta}(\xi, 0) = 0. \tag{3.14}$$

To complete the problem for Ψ_2, another boundary condition is required. This is the matching condition, which will be obtained in §5, namely

$$\Psi_2(\xi, \eta) \to \eta^2 \quad \text{as } \eta \to \infty. \tag{3.15}$$

It is observed that no elastic contribution appears to leading order. Equation (3.13) and its boundary conditions, (3.14) and (3.15), are exactly the same as in the case of a Newtonian fluid (Tillett 1968). A similarity solution for (3.13) was carried out by Tillett (1968) for Ψ_2, which is rewritten here as

$$\Psi_2(\xi, \eta) = \xi^{2/3} f_2(\theta), \tag{3.16}$$

where $\theta = \eta\xi^{-1/3}$ is the similarity variable. The equation for $f_2(\theta)$ is, from (3.13),

$$f_2''' + \frac{2}{3} f_2 f_2'' - \frac{1}{3} f_2'^2 = 0, \tag{3.17}$$

and the boundary conditions are, from (3.14) and (3.15),

$$f_2(0) = f_2''(0) = 0, \tag{3.18a}$$
$$f_2(\theta) \sim \theta^2 \quad \text{as } \theta \to \infty. \tag{3.18b}$$

Equation (3.17) can be solved numerically. Also, for large θ, the solution has the following asymptotic form (Tillett 1968):

$$f_2 = (\theta + c)^2 + O\left[\exp\left(-\frac{2}{9}\theta^3\right)\right], \tag{3.19}$$

where $c = 0.70798$ from the numerical integration. To the next order in ε, (3.6a) gives

$$\Psi_{2\eta}\Psi_{3\xi\eta} + \Psi_{3\eta}\Psi_{2\xi\eta} - \Psi_{2\xi}\Psi_{3\eta\eta} - \Psi_{2\eta\eta}\Psi_{3\xi} = \Psi_{3\eta\eta\eta}$$
$$+ aDe(\Psi_{2\eta\eta}\Psi_{2\xi\eta\eta} - \Psi_{2\eta}\Psi_{2\xi\eta\eta\eta} + \Psi_{2\xi}\Psi_{2\eta\eta\eta\eta} - \Psi_{2\xi\eta}\Psi_{2\eta\eta\eta}), \tag{3.20}$$

subject to the boundary conditions from (3.7a) and (3.7b), namely

$$\Psi_3(\xi, 0) = \Psi_{3\eta\eta}(\xi, 0) = 0. \tag{3.21a}$$

The matching condition from §5 is

$$\Psi_3(\xi, \eta) \sim -\frac{2}{3}\eta^3 \quad \text{as } \eta \to \infty, \tag{3.21b}$$

which completes the problem for Ψ_3. The (non-homogeneous) terms multiplied by aDe on the right-hand side of (3.20) constitute the viscoelastic contribution, which are written explicitly in terms of f_2 and its derivatives. Consequently, one may set

$$\Psi_3(\xi, \eta) = \xi f_3(\theta) + g_3(\theta), \tag{3.22}$$

where $g_3(\theta)$ accounts for non-Newtonian contribution. The term $\xi f_3(\theta)$ corresponds exactly to the Newtonian case (Tillett 1968). Substitution of expression (3.22) into

(3.20) yields two differential equations for f_3 and g_3. The f_3 equation is

$$f_3''' + \frac{2}{3}f_2 f_3'' - f_2' f_3' + f_2'' f_3 = 0, \tag{3.23}$$

with boundary conditions obtained from (3.21a), namely

$$f_3(0) = f_3''(0) = 0. \tag{3.24a}$$

The third boundary condition is obtained from (3.21b):

$$f_3(\theta) \sim -\frac{2}{3}\theta^3 \quad \text{as} \quad \theta \to \infty. \tag{3.24b}$$

Equation (3.23) is a linear equation that can be solved numerically. An asymptotic solution has been given by Tillett (1968) in the form

$$f_3(\theta) = -\frac{2}{3}[(\theta + c)^3 - 3] + B_3(\theta + c) + O\left[\exp\left(-\frac{2}{9}\theta^3\right)\right]. \tag{3.25}$$

The numerical integration of (3.22) gives the value $B_3 = -2.08913$. The g_3 equation turns out to be

$$g_3''' + \frac{2}{3}f_2 g_3'' = -\frac{2}{3}a De f_2 f_2^{\text{iv}}. \tag{3.26}$$

Two boundary conditions, namely the vanishing of g_3 and its second derivative at $\theta = 0$, are deduced from (3.21a). Obviously, a third boundary condition is needed in order to solve (3.26), which cannot be obtained from matching with the outer solution as in the case of f_2 and f_3. However, the asymptotic form (3.19) of f_2 indicates that the right-hand side of (3.26) vanishes as $\theta \to \infty$. In this case, g_3 must behave linearly at large θ. Thus, $g_3 = C_3\theta +$ constant at large θ. This condition will be used, in turn, to establish a direct relation between the slopes of g_3 at the origin and at infinity (see § 6), which constitutes the third boundary condition required to solve (3.26). It will be shown from matching (§ 5) that only the slope at large θ is needed, and the constant is therefore unimportant. Thus, the three boundary conditions needed to solve (3.26) turn out to be

$$g_3(0) = g_3''(0) = 0, \; g_3'(0) \simeq 1.806 g_3'(\infty). \tag{3.27}$$

Equation (3.26) indicates that $g_3(\theta)$ is proportional to aDe. The distributions of f_2, f_3 and g_3 are found upon integrating numerically (3.17), (3.23) and (3.26), respectively. Equation (3.26) is solved as an initial-value problem. The integration is carried out starting at $\theta = 0$, with a guessed value for $g_3'(0)$. A shooting method is used to refine the guess until condition (3.27) is met at large θ. Figure 2 displays the dependence of f_2, f_3 and g_3/aDe on θ. Although f_2 and f_3 are exactly the same as for a Newtonian jet, they are included here for reference. Indeed, g_3 reflects the influence of normal stress and deviation from Newtonian behaviour. The figure shows that g_3 and f_3 become comparable in magnitude for $aDe = O(10)$. In this case, the elasticity number $E = De/Re$ or, say, $E = aDe/Re = O(10\varepsilon^3)$. In fact, a smaller value of the Deborah number is sufficient for elastic effect to be significant for small distance to the exit. In fact, expression (3.22) suggests that elastic or normal stress effects are most significant close to the channel exit.

The expression for u in the inner region is obtained upon using expressions (3.11a), (3.16) and (3.22), leading to

$$u(x, \theta) = \varepsilon x^{1/3} f_2'(\theta) + \varepsilon^2 \left[x^{2/3} f_3'(\theta) + x^{-1/3} g_3'(\theta)\right]. \tag{3.28}$$
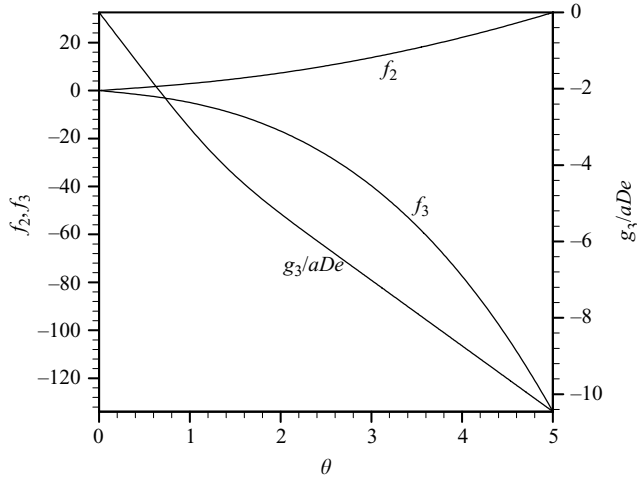
FIGURE 2. Dependence of the similarity functions f_2, f_3 and g_3 on θ.

Figure 3 displays the dependence of the streamwise velocity profiles on position (figure 3a) and elasticity (figure 3b) for $\varepsilon = 0.1$. These profiles allow, in turn, the determination of the boundary-layer thickness. Figure 3(a) shows the gradual flattening of the velocity profile with position and the simultaneous convergence, which is particularly evident from the saturation of the corresponding asymptotic profiles. The boundary-layer thickness $\delta(x)$, or equivalently the thickness of the inner region, coincides with the level at which the asymptotic and inner velocity profiles begin to merge. The boundary-layer thickness grows with position. Eventually, the inner region continues to grow with position as the jet contracts, and the flow approaches uniform conditions (see also §4.4), at which point the boundary layer prevails over the entire jet. Figure 3(b) indicates that the asymptotic solution tends to underestimate (overestimate) the velocity level for a flow with weak (strong) elasticity. The linear dependence of the velocity profiles on aDe is also apparent from expression (3.28). Finally, the thickness of the boundary layer increases with elasticity. This will be further confirmed in §6.

4. The flow in the core region (outer and channel regions)

It is convenient to define the core region as comprising the outer region outside the channel ($x > 0$) and the channel region upstream from the exit ($x < 0$). In the core region, which is far from the region near $z = 0$, ψ, p, q, r and s are represented by the following outer expansions:

$$\psi(x, z) = \psi_0(x, z) + \varepsilon \psi_1(x, z) + \ldots, \tag{4.1a}$$
$$p(x, z) = p_0(x, z) + \varepsilon p_1(x, z) + \ldots, \tag{4.1b}$$
$$q(x, z) = q_0(x, z) + \varepsilon q_1(x, z) + \ldots, \tag{4.1c}$$
$$r(x, z) = r_0(x, z) + \varepsilon r_1(x, z) + \ldots, \tag{4.1d}$$
$$s(x, z) = s_0(x, z) + \varepsilon s_1(x, z) + \ldots. \tag{4.1e}$$

Here, ψ_0, q_0, s_0 and r_0 are just the basic Poiseuille flow variables given in (2.9a)–(2.9d); ψ_k, q_k, s_k and r_k ($k > 0$) are higher-order terms that denote the deviation from the basic flow due to its interaction with the boundary layer. Since the governing equations are elliptic (in x), this deviation will extend also to the region $x < 0$ in the channel.
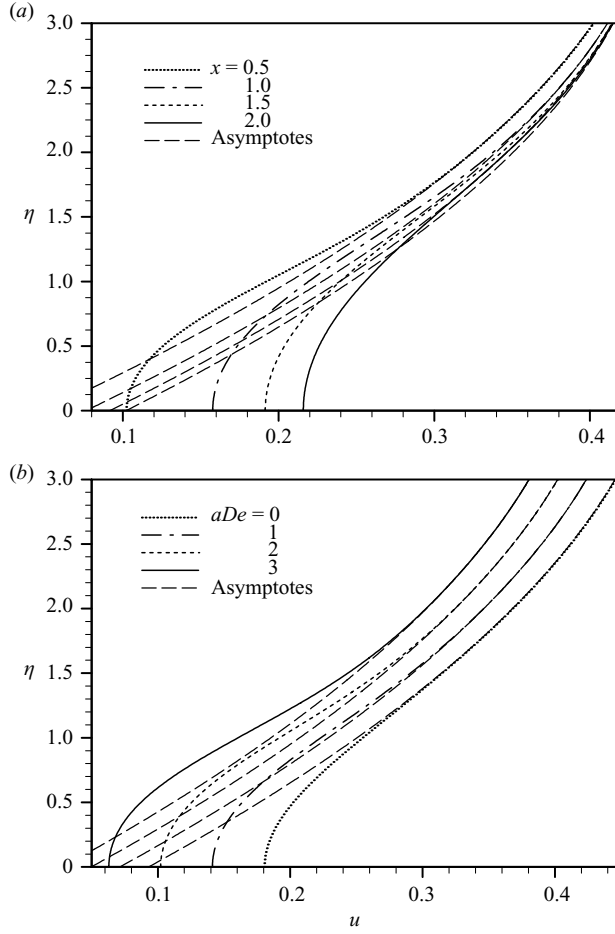
FIGURE 3. Dependence of the streamwise velocity profiles in the boundary-layer region for $\varepsilon = 0.1$ (a) on position at $aDe = 2$ and (b) on elasticity at $x = 0.5$. The dashed curves indicate asymptotic behaviour.

Based on these assumptions, upon inserting expressions (4.1) into (2.10a)–(2.10e) and noting that the leading-order flow variables, expressions (2.9a)–(2.9d), depend only on z, a hierarchy of equations is obtained to each order. To leading order the resulting equations for $k = 0$ lead to $p_0(x, z) = 0$. For $k = 1$, one has

$$\psi_{0z}\psi_{1xz} - \psi_{0zz}\psi_{1x} = -p_{1x}, \tag{4.2a}$$

$$-\psi_{0z}\psi_{1xx} = -p_{1z}, \tag{4.2b}$$

$$De\left(\psi_{0z}q_{1x} - \psi_{1x}q_{0z} - 2q_0\psi_{1xz} - 2s_0\psi_{1zz} - 2s_1\psi_{0zz}\right) + q_1 = 2a\psi_{1xz}, \tag{4.2c}$$

$$De\left(\psi_{0z}r_{1x} + 2s_0\psi_{1xx}\right) + r_1 = -2a\psi_{1xz}, \tag{4.2d}$$

$$De\left(\psi_{0z}s_{1x} - \psi_{1x}s_{0z} + q_0\psi_{1xx} - r_1\psi_{0zz}\right) + s_1 = a\left(\psi_{1zz} - \psi_{1xx}\right). \tag{4.2e}$$

Upon eliminating p_1 from (4.2a) and (4.2b), the following equation is obtained for ψ_1:

$$\nabla^2\psi_{1x} - \frac{\psi_{0zzz}}{\psi_{0z}}\psi_{1x} = 0, \tag{4.3}$$

where $\nabla^2 = (\partial^2/\partial x^2) + (\partial^2/\partial z^2)$. Noting that $w_1 = -\psi_{1x}$, the following boundary-value problem in the ranges $-\infty \leqslant x \leqslant \infty$ and $0 \leqslant z \leqslant 1/2$ is concluded:

$$
\left.
\begin{aligned}
&\nabla^2 w_1 + \tfrac{2}{z(1-z)} w_1 = 0, \\
&w_1\left(x, \tfrac{1}{2}\right) = 0, \\
&w_1(x, 0) = 0 && \text{for } x < 0, \\
&w_1(x, z \to 0) = -\lambda_1(x) && \text{for } x > 0, \\
&w_1 \quad \text{bounded as } |x| \to \infty.
\end{aligned}
\right\}
\tag{4.4}
$$

The matching condition obtained in §5 gives $\lambda_1 = 0$. In this case, the (unique) solution to the boundary-value problem (4.4) is $w_1(x, z) = 0$ for any x and z. Consequently, and since $\psi_1(x \to -\infty, z) = 0$, ψ_1, p_1, q_1, r_1 and s_1 must vanish everywhere. For $k = 2$, one has

$$
\psi_{0z}\psi_{2xz} - \psi_{0zz}\psi_{2x} = -p_{2x}, \tag{4.5a}
$$
$$
-\psi_{0z}\psi_{2xx} = -p_{2z}, \tag{4.5b}
$$
$$
De\left(\psi_{0z}q_{2x} - \psi_{2x}q_{0z} - 2q_0\psi_{2xz} - 2s_0\psi_{2zz} - 2s_2\psi_{0zz}\right) + q_2 = 2a\psi_{2xz}, \tag{4.5c}
$$
$$
De\left(\psi_{0z}r_{2x} + 2s_0\psi_{2xx}\right) + r_2 = -2a\psi_{2xz}, \tag{4.5d}
$$
$$
De\left(\psi_{0z}s_{2x} - \psi_{2x}s_{0z} + q_0\psi_{2xx} - r_2\psi_{0zz}\right) + s_2 = a\left(\psi_{2zz} - \psi_{2xx}\right). \tag{4.5e}
$$

Note that the terms including ψ_1, q_1, r_1 and s_1 vanish. Eliminating p_2 from (4.5a) and (4.5b) leads to a similar problem as in (4.4), where w_1 and λ_1 are now replaced by w_2 and λ_2, respectively. From matching (§5), it is also found that $\lambda_2 = 0$. This leads, in turn, to the vanishing of w_2 and, consequently, of ψ_2, p_2, q_2, r_2 and s_2 everywhere, similarly as before. For $k = 3$, the governing equations, (2.10a)–(2.10e), reduce to

$$
\psi_{0z}\psi_{3xz} - \psi_{0zz}\psi_{3x} = -p_{3x} - 4aRv + s_{0z}, \tag{4.6a}
$$
$$
-\psi_{0z}\psi_{3xx} = -p_{3z}, \tag{4.6b}
$$
$$
De\left(\psi_{0z}q_{3x} - \psi_{3x}q_{0z} - 2q_0\psi_{3xz} - 2s_0\psi_{3zz} - 2s_3\psi_{0zz}\right) + q_3 = 2a\psi_{3xz}, \tag{4.6c}
$$
$$
De\left(\psi_{0z}r_{3x} + 2s_0\psi_{3xx}\right) + r_3 = -2a\psi_{3xz}, \tag{4.6d}
$$
$$
De\left(\psi_{0z}s_{3x} - \psi_{3x}s_{0z} + q_0\psi_{3xx} - r_3\psi_{0zz}\right) + s_3 = a\left(\psi_{3zz} - \psi_{3xx}\right). \tag{4.6e}
$$

From matching, it is found that $\lambda_3 = 2$. In this case, using expressions (2.9a)–(2.9d) and eliminating p_3 from (4.6a) and (4.6b) lead to the following non-homogeneous problem:

$$
\left.
\begin{aligned}
&\nabla^2 w_3 + \frac{2}{z(1-z)} w_3 = 0, \\
&w_3\left(x, \tfrac{1}{2}\right) = 0, \\
&w_3(x, 0) = 0 && \text{for } x < 0, \\
&w_3(x, z \to 0) = -2 && \text{for } x > 0, \\
&w_3 \quad \text{bounded as } |x| \to \infty,
\end{aligned}
\right\}
\tag{4.7}
$$

where $w_3 = -\psi_{3x}$. The solution of problem (4.7) does not vanish given the non-homogeneity of the boundary conditions. So far, the formulation in this section has been common to the regions both inside and outside the channel. Although the flow fields in these two regions will have to match at the channel exit ($x = 0$), they can conveniently be examined separately.

4.1. *Flow in the channel region*

Consider now the core flow in the region $x < 0$. In this case, the solution of (4.7) may be written as (Tillett 1968)

$$w_3(x < 0, z) = -\psi_{3x}(x < 0, z) = -\sum_{n=1}^{\infty} A_n e^{\beta_n x} V_n(z). \tag{4.8}$$

The shape functions V_n are governed by the following eigenvalue problem:

$$V_n'' + \left[\beta_n^2 + \frac{2}{z(1-z)}\right] V_n = 0, \tag{4.9a}$$

$$V_n(0) = V_n\left(\frac{1}{2}\right) = 0, \tag{4.9b}$$

with β_n being real and positive (Tillett 1968). The coefficients A_n are obtained by matching the flow at the channel exit, which will be carried out in subsection 4.2. The pressure inside the channel is determined from (4.6b) subject to appropriate boundary conditions, which are obtained as follows. First recall from § 3 that the pressure in the inner region ($x > 0$) was shown to be $O(\varepsilon^4)$. Consequently, upon matching the pressures in the outer and inner regions, it is not difficult to deduce that the pressure in the outer region outside the channel vanishes at the interface or

$$p_3(x > 0, 0) = 0. \tag{4.10}$$

Thus, at the channel exit, this gives $p_3(0,0) = 0$. Now, upon evaluating (2.9a) and (2.9c) at $z = 0$ ($x < 0$), (4.6a) reduces to

$$p_{3x}(x, 0) = -4aRv - 4a = -4, \tag{4.11}$$

which is integrated subject to $p_3(0,0) = 0$ to give

$$p_3(x, 0) = -4x. \tag{4.12}$$

Upon inserting expressions (2.9a) and (4.8) into (4.6b), the expression for the transverse pressure gradient inside the channel becomes

$$p_{3z} = -2\sum_{n=1}^{\infty} \frac{A_n}{\beta_n} e^{\beta_n x}[z(1-z)V_n''(z) + 2V_n(z)], \tag{4.13}$$

which must be integrated subject to condition (4.12), leading finally to

$$p_3(x < 0, z) = -4x - 2\sum_{n=1}^{\infty} \frac{A_n}{\beta_n} e^{\beta_n x}[z(1-z)V_n' - 2(1-2z)V_n]. \tag{4.14}$$

Although the flow kinematics in the core region inside the channel, at least to $O(\varepsilon^3)$, is the same for both Newtonian and viscoelastic fluids, it is nevertheless useful to include some observations on the flow behaviour across the channel without actually showing any results. Although Poiseuille conditions are theoretically recovered in the limit $x \to -\infty$, calculations indicate that these conditions prevail essentially for $x < -1$, corresponding to a distance approximately of one channel width. Given the dominance of the leading term in (4.1a) and (4.1b), little deviation from the Poiseuille profile is expected. This is particularly true in the case of the streamwise velocity component and the pressure. The pressure remains essentially constant across the channel, except very close to the exit. A more significant deviation, at least qualitatively, is expected for the transverse velocity component.

The excess stress components can be determined upon substituting the expression for the stream function into the stress equations (4.6c)–(4.6e). The stream function (as well as the streamwise velocity component) is determined upon integrating (4.8) subject to $\psi_3 \to 0$ as $x \to -\infty$. The stress equations are solved subject to $q_3, r_3, s_3 \to 0$ as $x \to -\infty$ to give

$$q_3(x, z) = \sum_{n=1}^{\infty} \bar{Q}_n(z) e^{\beta_n x}, \tag{4.15a}$$

$$r_3(x, z) = \sum_{n=1}^{\infty} \bar{R}_n(z) e^{\beta_n x}, \tag{4.15b}$$

$$s_3(x, z) = \sum_{n=1}^{\infty} \bar{S}_n(z) e^{\beta_n x}, \tag{4.15c}$$

where

$$\bar{Q}_n(z) = \frac{1}{1 + \beta_n De\psi_{0z}} \left[De \left(A_n q_{0z} V_n + 2A_n q_0 V_n' + \frac{2s_0 A_n V_n''}{\beta_n} + 2\psi_{0zz} \bar{S}_n \right) + 2a A_n V_n' \right], \tag{4.16a}$$

$$\bar{R}_n(z) = -\frac{2A_n}{1 + \beta_n De\psi_{0z}} (Des_0 \beta_n V_n + a V_n'), \tag{4.16b}$$

$$\bar{S}_n(z) = \frac{1}{1 + \beta_n De\psi_{0z}} \left[-De\psi_{0zz} \bar{R}_n + De A_n (s_{0z} - \beta_n q_0) V_n + a A_n \left(\frac{V_n''}{\beta_n} - \beta_n V_n \right) \right]. \tag{4.16c}$$

Expressions (4.15) will be used below to assess the influence of elasticity on stress along the centreline.

4.2. *Flow in the outer region*

Downstream from the channel exit, Tillett's solution is rewritten here as

$$w_3(x > 0, z) = -\psi_{3x}(x > 0, z) = -2V_0(z) + \sum_{n=1}^{\infty} A_n e^{-\beta_n x} V_n(z), \tag{4.17}$$

where

$$V_0(z) = 1 - 2z - 2z(1 - z) \ln \frac{z}{1 - z}. \tag{4.18}$$

As mentioned earlier, the coefficients A_n are obtained by matching w_3 at $x = 0$. It is not difficult to show from (4.8) and (4.17), given the orthogonality of the shape functions V_n, that

$$A_n = \frac{\int_0^{1/2} V_0(z) V_n(z) \, dz}{\int_0^{1/2} V_n^2(z) \, dz}. \tag{4.19}$$

Incidentally, the A_n values given by Tillett (1968) are incorrect. These values are, however, easy to reproduce and will not be given explicitly here. An expression for the pressure can be obtained in the outer region similar to the channel region. In this case,

$$p_3(x > 0, z) = -2 \sum_{n=1}^{\infty} \frac{A_n}{\beta_n} e^{-\beta_n x} [z(1 - z) V_n' - 2(1 - 2z) V_n]. \tag{4.20}$$
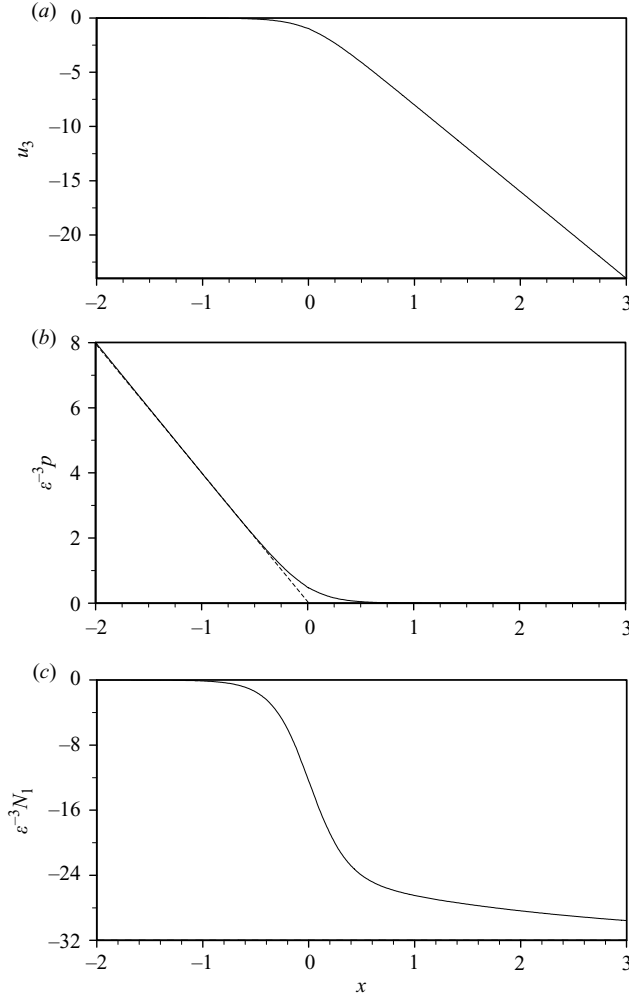
FIGURE 4. Flow and stress behaviour along the centreline. The (streamwise) velocity, pressure and primary normal stress difference are shown in (*a*), (*b*) and (*c*), respectively. Here $\varepsilon = 0.3$, $a = 0.25$ and $De = 4$.

The expressions for the stress components in the outer region outside the channel ($x > 0$) can be determined upon solving (4.6*c*)–(4.6*e*) and matching with expressions (4.15) at $x = 0$. These expressions are not difficult to obtain but are cumbersome. For this reason, they will be given next only along the centreline $z = 1/2$.

4.3. *Flow along the centerline*

The flow along the centreline $z = 1/2$ is interesting to examine, as it provides insight on the flow transition as the fluid exits the channel. Figure 4 displays the deviation of the streamwise velocity from the basic flow (figure 4*a*), the pressure (figure 4*b*) and primary normal stress difference (figure 4*c*) along the centreline. Note that the normal stress difference includes the Newtonian contribution. Poiseuille conditions for velocity and pressure appear to be reached when $x < -0.5$. Most of the deviation in velocity occurs outside the channel. In fact, the velocity decreases slightly from the Poiseuille level for $x < 0$, indicating a flattening of the velocity profile as the exit

is approached. The velocity continues to decrease faster (essentially linearly) with x outside the channel. This behaviour is inferred from the expression for $u(x, z)$, which is obtained by integrating expressions (4.8) and (4.17), matching at $x = 0$ and using (4.1*a*). At the centreline, this gives

$$u\left(x, z = \frac{1}{2}\right) = \begin{cases} \dfrac{1}{2} + \varepsilon^3 \displaystyle\sum_{n=1}^{\infty} \dfrac{A_n}{\beta_n} \, e^{\beta_n x} V_n'\left(\dfrac{1}{2}\right) & (x < 0), \\[3ex] \dfrac{1}{2} - \varepsilon^3 \left[8x - \displaystyle\sum_{n=1}^{\infty} \dfrac{A_n}{\beta_n} e^{-\beta_n x} V_n'\left(\dfrac{1}{2}\right)\right] & (x > 0). \end{cases} \tag{4.21}$$

This expression shows that the velocity decreases like $-8\varepsilon^3 x$ at large $x > 0$. Simultaneously, the pressure distribution in figure 4(*b*) confirms that Poiseuille conditions are recovered at $x \approx -0.5$. The pressure decays with x, reaching zero level outside the channel, at a distance slightly smaller than one channel width ($x \approx 0.8$), based on (4.20). Interestingly, the linear decay in velocity occurs at a position closer to the exit ($x \approx 0.5$). The expression for the (primary) normal stress difference on the centreline inside the channel reads

$$N_1\left(x < 0, z = \frac{1}{2}\right) = 4a\varepsilon^3 \sum_{n=1}^{\infty} \left(Rv + \frac{2}{2 + \beta_n De}\right) A_n \, e^{\beta_n x} V_n'\left(\frac{1}{2}\right), \tag{4.22a}$$

whereas that outside the channel reduces to

$$N_1\left(x > 0, z = \frac{1}{2}\right) = -32\varepsilon^3 - 4a\varepsilon^3 \sum_{n=1}^{\infty} \left(Rv + \frac{2}{2 - \beta_n De}\right) A_n \, e^{-\beta_n x} V_n'\left(\frac{1}{2}\right)$$

$$+ 32a\varepsilon^3 \left[1 + \sum_{n=1}^{\infty} \frac{A_n}{4 - (\beta_n De)^2} V_n'\left(\frac{1}{2}\right)\right] e^{-\frac{2x}{De}}. \tag{4.22b}$$

The primary normal stress difference in figure 4(*c*), which is shown for $De = 4$ and $a = 0.25$, indicates that the stress relaxes to the Poiseuille level at a distance further upstream from the channel exit ($x \approx -1$), in comparison to the velocity and pressure. The normal stress experiences a sharp gain at $x = 0$. It is interesting to note that this gain is caused mainly by Newtonian and not elastic elongation of the flow as it traverses the exit. In fact, the stress relaxes to the Newtonian level ($N_1 = -32\varepsilon^3$) at a relatively short distance downstream from the exit (see expression (4.22*b*)). The overall influence of elasticity on the normal stress difference along the centreline is depicted in figure 5 for the range $De \in (0, 5]$. The effect of elasticity seems rather weak in the channel region. For large $x > 0$, the stress relaxes less rapidly to the Newtonian level as De increases. There is, however, a saturation effect of elasticity that can be inferred from figure 5 and expressions (4.22) for large De. More importantly, elasticity tends to diminish the normal stress level. This may seem counterintuitive at first. However, examination of the stress level near the free surface (see §7) will indeed confirm the overall increase of normal stress effect with increase of the Deborah number.

4.4. *Contraction ratio of the viscoelastic jet*

This section is concluded by utilizing the outer solution to compute the final velocity W and the final contraction ratio χ of the jet far downstream from the exit. The
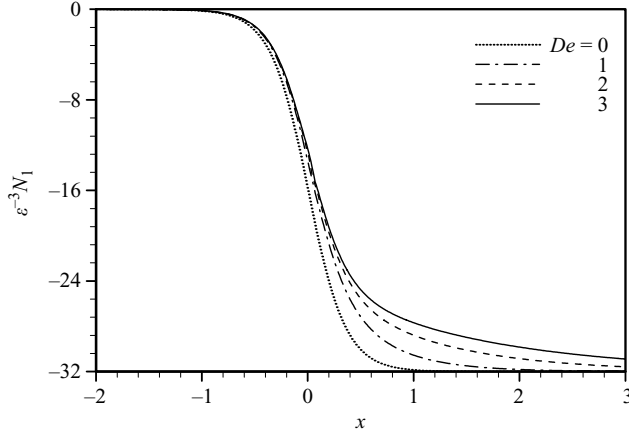
FIGURE 5. Influence of elasticity on the primary normal stress difference along the centreline for $a = 0.25$.
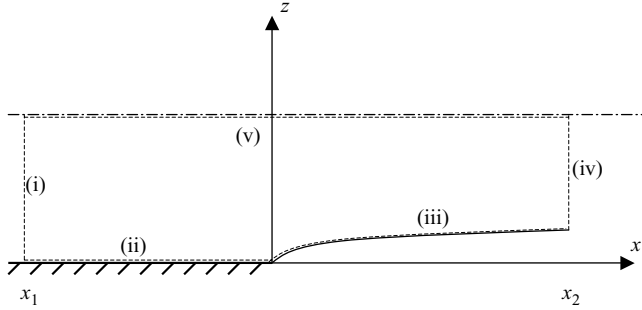
FIGURE 6. Control volume used in the evaluation of contour integral (4.23).

non-dimensional momentum equation may be written in integral form as

$$\int_C (\boldsymbol{\sigma} - \boldsymbol{uu}) \cdot \boldsymbol{n}l = 0, \tag{4.23}$$

where $\boldsymbol{u}$ is the velocity vector and $\boldsymbol{\sigma}$ is total stress tensor given by

$$\boldsymbol{\sigma} = -p\boldsymbol{I} + \varepsilon^3 a Rv(\nabla \boldsymbol{u} + \nabla \boldsymbol{u}^t) + \varepsilon^3 \boldsymbol{\tau}, \tag{4.24}$$

where $\boldsymbol{\tau}$ is the non-dimensional polymeric stress tensor. Here $\mathrm{d}l$ denotes a line element of the closed curve C, which is taken to consist of the following arcs: (i) a line $x = x_1 < 0$, $0 \leqslant z \leqslant 1/2$ upstream; (ii) a segment $x_1 \leqslant x \leqslant 0$, $z = 0$ of the lower wall; (iii) a segment $0 \leqslant x \leqslant x_2$, $z = \zeta(x)$ of the lower free streamline; (iv) a line $x = x_2$, $\zeta(x_2) \leqslant z \leqslant 1/2$ downstream; (v) the segment $x_1 \leqslant x \leqslant x_2$, $z = 1/2$ of the centreline (see figure 6). Only the x component of (4.23) is considered. Thus, (iii) and (v) will not make any contribution. In the limit $x_2 \to \infty$, one obtains

$$\int_0^{1/2} [(p - 2\varepsilon^3 a Rv\psi_{xz} - \varepsilon^3 q) + \psi_z^2]_{x=x_1} \mathrm{d}z - \int_{x_1}^0 \varepsilon^3 [aRv\psi_{zz}(x, 0) + s] \, \mathrm{d}x - \frac{1}{2} W^2 \chi = 0. \tag{4.25}$$

From (4.14) it can be deduced that as $x_1 \to -\infty$, $p \to -4\varepsilon^3 x_1$. Note that in this limit, also $\psi \to \psi_0$ and $q \to q_0$. Thus, there is a cancellation between the pressure of the

basic Poiseuille flow and its integrated skin friction, leaving

$$\frac{1}{2}W^2\chi = \int_0^{1/2} \left(\psi_{0z}^2 - \varepsilon^3 q_0 \right)_{x=x_1} \mathrm{d}z + o(\varepsilon^3), \tag{4.26}$$

which, upon use of (2.9a) and (2.9d), leads to

$$\frac{1}{2}W^2\chi = \frac{1}{15} - \frac{4}{3}\varepsilon^3 aDe + o(\varepsilon^3). \tag{4.27}$$

From conservation of mass, one has

$$W\chi = \frac{1}{3}. \tag{4.28}$$

Finally, from (4.27) and (4.28), the contraction ratio and the velocity far downstream are obtained explicitly in terms of the Reynolds and Deborah numbers, as well as the viscosity ratio, as

$$\chi = \frac{5}{6}(1 + 20\varepsilon^3 aDe) + o(\varepsilon^3), \tag{4.29}$$

$$W = \frac{2}{5} - 8\varepsilon^3 aDe + o(\varepsilon^3). \tag{4.30}$$

Clearly, expression (4.29) indicates that elasticity tends to prohibit contraction. The jet contraction ratio increases linearly with aDe. Interestingly, (4.29) reveals the intricate interplay among inertial, viscous and normal stress effects. Also of interest here is the fact that in contrast to a viscoelastic jet, the contraction of a Newtonian jet does not depend on inertia to the order of the present analysis (with a contraction ratio $\chi = 5/6$). Of course, this is the case of a jet at relatively high Reynolds number. The contraction ratio, χ, increases with aDe at a rate of $(50/3)\varepsilon^3$. The contraction ratio of the jet close to the exit will be discussed later once the matching process is carried out and the composite solution is obtained.

5. Matching process

The matching rule employed by Van Dyke (1964) is adopted here, namely

$$E_n H_m \psi = H_m E_n \psi, \tag{5.1}$$

where m and n are integers. Here, E_n is the outer-expansion operator, which truncates immediately after the term of order ε^n where the expansion is expressed in terms of outer variables; H_m is the corresponding inner-expansion operator. For successful application of the matching rule (5.1), the stretching transformation between the inner and outer variables must be in the canonical form $y = \varepsilon\eta$. In this case, the outer expansion must be written in terms of y, not z; otherwise (5.1) can be satisfied only approximately. It is required that the two expressions in (5.1) be exactly the same, for all m and n.

Recall that to leading order, the stream function in the outer region is $\psi_0 = z^2 - (2/3)z^3$, which can be expressed in terms of y and h as (see §3)

$$\psi = (y + \varepsilon h)^2 - \frac{2}{3}(y + \varepsilon h)^3. \tag{5.2}$$

Consider first $m = 2$ and $n = 0$. Applying E_0 on (5.2) gives

$$E_0\psi = y^2 - \frac{2}{3}y^3. \tag{5.3}$$

As this expression must be in inner variables when the operator H_2 is applied, $E_0\psi$ is rewritten in the form

$$E_0\psi = \varepsilon^2\eta^2 - \frac{2}{3}\varepsilon^3\eta^3. \tag{5.4}$$

Therefore,

$$H_2 E_0\psi = \varepsilon^2\eta^2 = y^2. \tag{5.5}$$

To leading order, the inner expansion for the stream function is obtained from (3.8) as $\psi = \varepsilon^2\Psi_2$. This leads to $\Psi_2 \sim \eta^2$ for large η, which is condition (3.15) or equivalently (3.18b). Recall that this condition led to the determination of f_2. Consequently, from (3.8), (3.16) and (3.19), at large θ

$$H_2\psi = \varepsilon^2\Psi_2 = \varepsilon^2\xi^{2/3} f_2 = \varepsilon^2\xi^{2/3}(\theta + c)^2 = \varepsilon^2\xi^{2/3}(\eta\xi^{-1/3} + c)^2. \tag{5.6}$$

When (5.6) is expressed in terms of outer variables, it becomes

$$H_2\psi = (y + \varepsilon cx^{1/3})^2 = y^2 + 2y\varepsilon cx^{1/3} + \varepsilon^2(cx^{1/3})^2, \tag{5.7}$$

leading to

$$E_0 H_2\psi = y^2, \tag{5.8}$$

as required. So it can be seen that for $n = 0$ and $m = 2$, the inner and outer expansions match, and (5.1) is satisfied. Similarly, taking $n = 0$ and $m = 3$ leads to

$$H_3 E_0\psi = \varepsilon^2\eta^2 - \frac{2}{3}\varepsilon^3\eta^3, \tag{5.9}$$

which, in turn, leads to $\Psi_3 \sim -(2/3)\eta^3$ and consequently to condition (3.24b). Next, (5.1) is considered with $m = 2$ and $n = 1$. In this case, from (2.9a), (3.1), (3.9) and (4.1a),

$$E_1\psi = y^2 - \frac{2}{3}y^3 + \varepsilon[\psi_1(x, y + \varepsilon h) + 2(y - y^2)h_0(x)]. \tag{5.10}$$

Expanding about y, (5.10) reduces to

$$E_1\psi = y^2 - \frac{2}{3}y^3 + \varepsilon[\psi_1(x, y) + 2(y - y^2)h_0(x)]. \tag{5.11}$$

In this case, noting that $y = \varepsilon\eta$ is small, one has

$$\begin{aligned} H_2 E_1\psi &= \varepsilon\psi_1(x, 0) + \varepsilon^2(\eta^2 + \eta\psi_{1y}(x, 0) + 2\eta h_0(x)) \\ &= y^2 + \varepsilon[\psi_1(x, 0) + y\psi_{1y}(x, 0) + 2yh_0(x)]. \end{aligned} \tag{5.12}$$

On the other hand, applying $E_1 H_2$ on the inner expansion (3.8) and using (5.7) give

$$E_1 H_2\psi = E_1(\varepsilon^2\Psi_2) = y^2 + 2\varepsilon cyx^{1/3}. \tag{5.13}$$

Comparing (5.12) and (5.13) leads to $\psi_1(x, 0) = 0$. This leads in turn to the homogeneous boundary condition $\lambda_1(x) = -\psi_{1x}(x, 0) = 0$ for problem (4.4). Since $\psi_1 = 0$ everywhere is a solution for this problem (see §4), one concludes that $\psi_{1y}(x, 0) = 0$. The remaining terms in (5.12) and (5.13) then yield the result $h_0(x) = cx^{1/3}$. In this case, recalling that $c = 0.70798$, the free-surface height is given by

$$\zeta(x) = 0.70798\varepsilon x^{1/3} + O(\varepsilon^2). \tag{5.14}$$

The vanishing of $\psi_1(x, z)$ means that to the order ε, there is no interaction between the boundary layer and the outer flow. Obviously, no elastic or normal stress effect intervenes to this order. The form of $h_0(x)$ obtained also ensures that (5.1) is satisfied

for $m=3$ and $n=1$. The next step is to determine $\psi_2(x,z)$ and $h_1(x)$ by considering a matching process analogous to the one above, using $m=n=2$. By applying H_2E_2 to the outer expansion (4.1a) and E_2H_2 to the inner expansion (3.8), one has

$$H_2E_2\psi = y^2 + 2\varepsilon yh_0 + \varepsilon^2 \left(h_0^2 + \psi_2(x,0)\right) \tag{5.15}$$

and

$$E_2H_2\psi = y^2 + 2c\varepsilon yx^{1/3} + c^2\varepsilon^2 x^{2/3}. \tag{5.16}$$

This yields the fact that $\psi_2(x,0)=0$ in the outer expansion, concluding that $\psi_2(x,z)=0$, reflecting the absence of interaction between the boundary layer and the outer flow also to the order ε^2. The next step is to determine $h_1(x)$ and $\psi_3(x,0)$. Upon using expressions (3.8), (3.16) and (3.22), for $n=m=3$, one obtains

$$E_3H_3\psi = y^2 - \frac{2}{3}y^3 + 2\varepsilon\left(y-y^2\right)cx^{1/3} + \varepsilon^2\left[(1-2y)c^2x^{2/3} + B_3yx^{2/3} + C_3yx^{-1/3}\right]$$
$$+ \varepsilon^3\left(-\frac{2}{3}c^3x + B_3cx + 2x + C_3c\right). \tag{5.17}$$

Applying H_3E_3 to the outer expansion (4.1a) gives in turn

$$H_3E_3\psi = y^2 - \frac{2}{3}y^3 + 2\varepsilon\left(y-y^2\right)h_0 + \varepsilon^2\left[(1-2y)h_0^2 + 2yh_1\right]$$
$$+ \varepsilon^3\left(-\frac{2}{3}h_0^3 + 2h_0h_1 + \psi_3(x,0)\right). \tag{5.18}$$

Upon matching, the height of the free surface to the next order, h_1, is determined. Also, the boundary condition, which is required to complete the set of boundary conditions in (4.7), is obtained. Thus,

$$h_1 = \frac{1}{2}\left(B_3x^{2/3} + C_3x^{-1/3}\right), \tag{5.19}$$

$$\psi_3(x,0) = 2x. \tag{5.20}$$

Condition (5.20) yields that $\lambda_3=2$ in (4.7). Therefore, for the first time, a non-trivial outer problem is reached. It can be concluded that the outer flow up to order ε^3 remains the same as the Newtonian flow. However, the important result reached here from the matching process is that the height of the free surface is no longer the same as the Newtonian case and is given by

$$\zeta(x) = \varepsilon cx^{1/3} + \frac{1}{2}\varepsilon^2\left(B_3x^{2/3} + C_3x^{-1/3}\right), \tag{5.21}$$

where c and B_3 are known constants, whereas C_3, which embodies elastic behaviour, remains unknown at this stage but will be determined in the next section.

6. Flow very close to the channel exit and jet profile

Upon setting $\theta=0$ in (3.28), an expression is obtained for the streamwise velocity component at the free surface, $u(x,z=\zeta)$. Inspection of this expression and expression (5.21) for the free-surface height readily indicates that these expansions break down in the limit $x\to0$. This situation is reminiscent of that corresponding to Newtonian flow when higher-order terms are included in the boundary-layer region (see §7 in Tillett 1968). It is important to observe, however, that although the Newtonian expansions for streamwise velocity and surface height do not display a singularity at the origin

up to second order, the slope in height as well as the streamwise velocity gradient (rate of elongation) and, consequently, the transverse velocity component all become singular at $x = 0$. It is therefore expected that for viscoelastic jet flow, the breakdown in velocity gradient should lead to a breakdown in stress and ultimately in velocity (and surface height) because of the coupling between stress and flow. The situation is remedied by assuming the existence of a region, $0 < x < x_*$, near the origin within which the inner flow and stress expansions (3.8), (3.9) and (3.11) cease to be valid.

6.1. *Evaluation of x_**

The distance $[0, x_*]$ is expected to be small and indeed turns out to be of the order of the boundary-layer thickness (see below). In addition, x_* can be determined by first observing that the leading-order terms in (3.28) and (5.21) indicate that both the free-surface velocity and free-surface height must predominantly remain close to zero as $x \to 0$. It is therefore reasonable to assume that very close to the channel exit, the change in free-surface velocity and height is negligible (see Shi, Breuer & Durst 2004). Thus, set

$$\varepsilon x_*^{1/3} f_2'(0) + \varepsilon^2 \left[x_*^{2/3} f_3'(0) + x_*^{-1/3} g_3'(0) \right] = 0, \tag{6.1}$$

$$\varepsilon c x_*^{1/3} + \frac{1}{2}\varepsilon^2 \left(B_3 x_*^{2/3} + C_3 x_*^{-1/3} \right) = 0. \tag{6.2}$$

Recall that C_3 and $g_3'(0)$ are yet to be determined. Recall also that $g_3'(\theta \to \infty) = C_3$. Thus, the solution of (6.1) and (6.2) will allow the determination of x_* and the establishment of a relation between C_3 and $g_3'(0)$ or equivalently the third boundary condition in (3.27) required to solve (3.26). Since x_* is small, one may write

$$x_* = x_1 \varepsilon^\beta + x_2 \varepsilon^{2\beta} + \dots, \tag{6.3a}$$

where β is unknown for now. Consequently, inspection of (6.1) and (6.2) leads to the following expansions:

$$g_3'(0) = g_{30}'(0) + g_{31}'(0)\varepsilon^\beta + \dots, \tag{6.3b}$$

$$C_3 = C_{30} + C_{31}\varepsilon^\beta + \dots. \tag{6.3c}$$

Upon substituting (6.3) into (6.1) and (6.2), it is not difficult to conclude that in order to have a balance among the terms in both equations, one should set $\beta = 3/2$. In this case, (6.1) gives, to leading order in (6.3a),

$$x_1 = \left(-\frac{g_{30}'(0)}{f_2'(0)} \right)^{3/2}. \tag{6.4}$$

This leads, in turn, upon substitution into (6.2) to the relation

$$g_{30}'(0) = \frac{C_{30} f_2'(0)}{2c} = 1.806 C_{30} \tag{6.5}$$

between C_{30} and $g_{30}'(0)$, which is used approximately as the third boundary condition in (3.27). From the numerical solution of (3.26) one finds $C_3 \simeq C_{30} = -1.72 a De$. The value of $\beta = 3/2$ is confirmed by assessing the weight of terms in the original equation of motion, (2.10) in the inner region, which is rewritten here as

$$Re \left[u \left(u_x - \left(\frac{\theta}{3x} + \frac{h'}{x^{1/3}} \right) u_\theta \right) - \frac{1}{\varepsilon x^{1/3}} w u_\theta \right]$$
$$= aRv \frac{1}{\varepsilon^2 x^{2/3}} u_{\theta\theta} + q_x - \left(\frac{\theta}{3x} + \frac{h'}{x^{1/3}} \right) q_\theta - \frac{1}{\varepsilon x^{1/3}} s_\theta. \tag{6.6}$$

The region of validity of the boundary-layer solution in the inner region can be estimated as follows. To leading order, near the free surface (inner region), the streamwise velocity and normal stress, as well as the shear stress components and free-surface height, are recalled from §§ 3 and 5 as

$$u \approx \varepsilon x^{1/3} f_2'(\theta), \quad q \approx 2aDe\left[f_2''(\theta)\right]^2, \quad s \approx af_2''(\theta), \quad h = cx^{1/3}. \tag{6.7}$$

This solution is applicable close to the exit, including $x = 0$, since it does not exhibit any singularity. Using these expressions and upon balancing the inertial, viscous and elastic terms in (6.6), one has

$$\varepsilon^{-1}x_*^{-1/3} \sim \varepsilon x_*^{1/3}\delta_*^{-2} \sim x_*^{-1}aDe. \tag{6.8}$$

This relation is equivalent to two equations with two unknowns, namely the position, x_*, at which (6.7) becomes valid and the corresponding value of the boundary-layer thickness, $\delta_* \equiv \delta(x = x_*)$, at that position. Solving leads to

$$x_* \sim \varepsilon^{3/2}(aDe)^{3/2}, \quad \delta_* \sim \varepsilon^{3/2}\sqrt{aDe}. \tag{6.9}$$

The first estimate in (6.9) confirms the validity of expansion (6.3). Interestingly, this estimate indicates that x_1 in (6.3) increases like $(aDe)^{3/2}$, which, in turn, confirms from (6.4) that $g_3'(0)$ behaves like aDe. More importantly, both x_* and δ_* are of the same order of magnitude, which is typical of boundary-layer flows. In other words, this confirms that the boundary-layer approximation is valid only beyond a distance from the channel exit that is of the order of the boundary-layer thickness.

6.2. *Boundary-layer thickness very close to channel exit*

A more accurate estimate of the boundary-layer thickness at any position is obtained numerically using expression (3.28) for the streamwise velocity component in the inner region and its asymptotic counterpart for large θ, namely

$$u(x, \theta \to \infty) = 2\varepsilon x^{1/3}(\theta + c) + \varepsilon^2[x^{2/3}(B_3 - 2\theta^2 - 4c\theta - 2c^2) + x^{-1/3}C_3]. \tag{6.10}$$

Note in this case that the boundary-layer thickness depends on the similarity group aDe and ε. Figure 7 displays the dependence of δ_* on inertia and elasticity. The plots show that the boundary-layer thickness increases with elasticity and decreases with inertia. Figure 7(a) displays the dependence of δ_* on ε for three aDe values. Note that the limit $\delta_*(\varepsilon = 0) = 0$ corresponds to the inviscid limit, where no boundary layer exists. The inset in figure 7(a) indicates that the slope in the log–log plots is sensibly the same and is approximately equal to 1.55. The numerical results in figure 7(b) give a slope of approximately 0.51, independent of the Reynolds number, confirming the universal dependence of the boundary-layer thickness on elasticity. One thus arrives at the following behaviour for the boundary-layer thickness near the channel exit:

$$\delta_* \simeq C\varepsilon^{1.55}(aDe)^{0.51}, \tag{6.11}$$

where C is a constant. In this case, (6.11) confirms the behaviour predicted in (6.9) based on dimensional arguments.

6.3. *Jet profile*

Figure 8 shows the dependence of the free-surface height on elasticity. It is interesting to note that aDe appears as the only parameter; a and De do not appear separately. This is easily inferred from expressions (5.21) and figure 2 (with the latter showing that $g_3'(0)$ and, therefore, C_3 depend on aDe). As expected, the jet contracts for any Deborah number given the presence of relatively high inertia. However, the effect
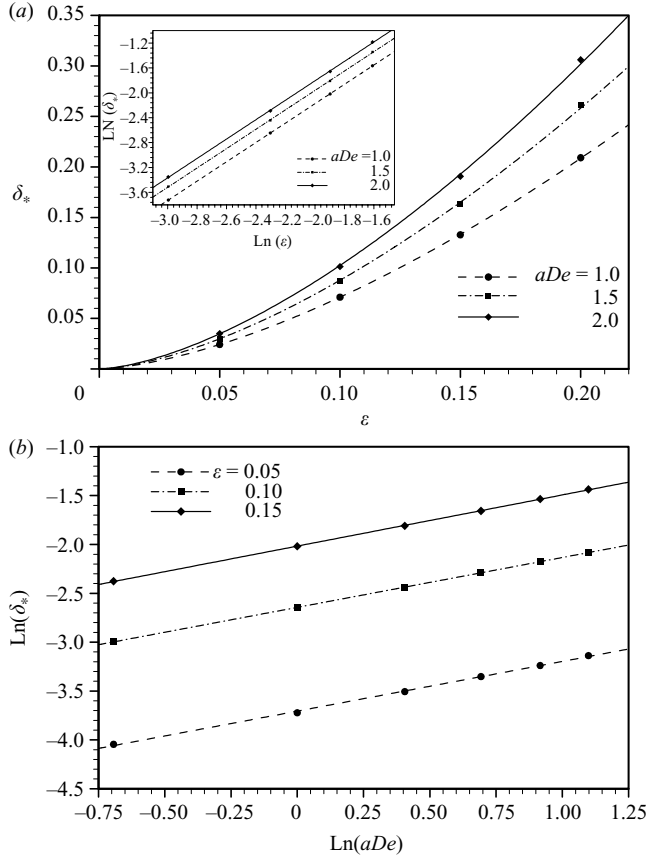
FIGURE 7. Dependence of boundary-layer thickness on (*a*) inertia and (*b*) elasticity at $x = x_*$.

of normal stress is significant. Elasticity tends to delay the contraction further downstream from the channel exit, in comparison with a Newtonian jet, which contracts at $x = 0$. In addition, the contraction is weakened by normal stress. Incidentally, the contraction ratio close to the exit can be inferred from figure 8. Figure 9 compares the contraction ratio at infinity to that at $x = 2$. The figure indicates that the contraction ratio at $x = 2$ (or essentially any x) also increases linearly with the Deborah number, at a slope equal to 0.0134 for $\varepsilon = 0.1$ in comparison with 0.0168 based on expression (4.29). Finally, the distributions of the velocity components can be obtained along the free surface by setting $\theta = 0$. The expression for $u(x, z = \zeta)$ is given from (3.28), whereas that for $w(x, z = \zeta)$ is deduced from (3.8) and (5.21) to give

$$w(x, \theta = 0) = \frac{\varepsilon^2}{3} c x^{-1/3} f_2'(0) + \frac{\varepsilon^3}{3} (c f_3'(0) + B_3 f_2'(0)) + o(\varepsilon^3). \tag{6.12}$$

Note that because of (6.5), $w(x, z = \zeta)$ turns out to be independent of elasticity, as reflected in figure 8. There is close qualitative similarity between the ζ and u distributions (not shown here).

For relatively large *De*, the straight segment of the jet in figure 8, or x_*, is expected to lengthen further, and the contraction is expected to eventually give way to swelling. This is the delayed swell scenario, where normal stress effect is strong with inertia remaining moderate. The swell occurs closer to the exit if elasticity is further increased.
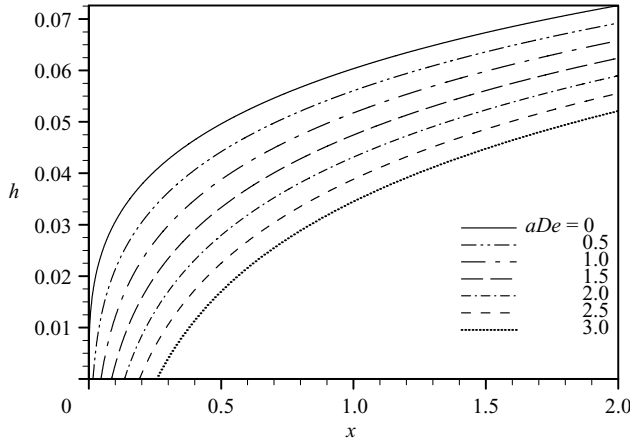
FIGURE 8. Influence of elasticity on free-surface profiles for $\varepsilon = 0.1$. Note that the surface profile depends only on the similarity parameter aDe.
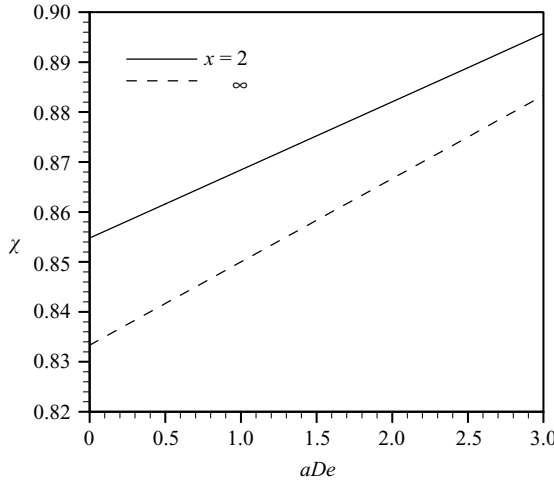
FIGURE 9. Dependence of the contraction ratio on elasticity close to the channel exit $(x = 2)$ and far from the exit for $\varepsilon = 0.1$.

Delayed swell appears to be caused by some inertial mechanism (Cloitre *et al.* 1998). Obviously, the whole range of normal stress effect cannot be captured by the present formulation, which is adequate for a flow with dominant inertia and $De = O(1)$. Of course, in the absence of inertia, the swell occurs right at the channel exit (Tanner 1999).

6.4. *Comparison with gravity-driven flow measurements*

Of closer relevance to the present results are the measurements reported by Liang *et al.* (1999). Although their study focused on the interplay between gravity and normal stress effects, some qualitative comparison with the present results is possible, since gravity plays a somewhat similar role to inertia. Note, however, the absence of inertia in their experiment, with $Re = O(10^{-5}–10^{-3})$. Referring back to figure 8, one observes the jet profiles reported for a range of Deborah number, $0 \leqslant aDe \leqslant 3$. For very small De, the jet contracts right at the channel exit. This is the necking phenomenon, which
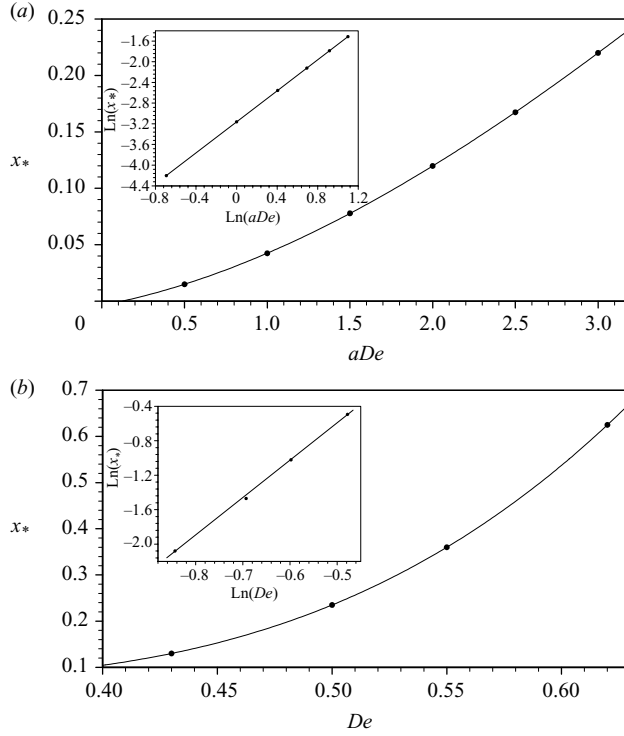
FIGURE 10. Influence of elasticity on the transition length, x_*. Theoretical values are shown in (*a*) for $\varepsilon = 0.1$. Experimental values from Liang *et al.* (1999) are shown in (*b*). Insets depict the corresponding logarithmic values.

is typical of Newtonian jet flow at moderate Reynolds number. This behaviour was also observed by Liang *et al.* (1999) in their greyscale images in figure 2(*a*). As *De* increases, figure 8 shows that the jet height near the exit becomes of the same level as the channel height. This situation is similar to that reported by Liang *et al.* (1999) in figure 2(*b*) of their work for $De = 0.55$. For larger *De* value, their figure 2(*c*) shows that the jet has larger diameter than that of the pipe at the exit. Referring to the jet profiles in figure 4 of Liang *et al.* (1999), one can observe the influence of normal stress over a wide interval of the Deborah number, ranging from the purely elastic regime, where die swell is observed, to the gravity dominant regime, where necking is observed. Some direct comparison is now carried out with their results.

Of particular interest to the present work are the jet profiles in the range $0.43 \leqslant De \leqslant 0.62$ in figure 4 of Liang *et al.* (1999), which should be compared with the profiles of figure 8 above. In this range of Deborah number, the experimental jet profiles of Liang *et al.* (1999) exhibit a flat region near the exit, reflecting the balance between elastic and gravity effects, similar to the balance between elasticity and inertial effects in the present problem. At a distance beyond the flat region, say x_*, contraction is observed. These experimental profiles are now used to estimate the dependence of the experimental x_* value on elasticity and compare it to the current theory. The comparison is shown in figure 10, which displays the dependence of x_* on *aDe*. Figure 10(*a*) shows the theoretical values obtained numerically by solving (3.17) and (3.26) and the use of (6.3*a*) and (6.4). The log–log plot in the inset of the figure suggests that x_* increases with elasticity like $De^{3/2}$, confirming the result in (6.9) based
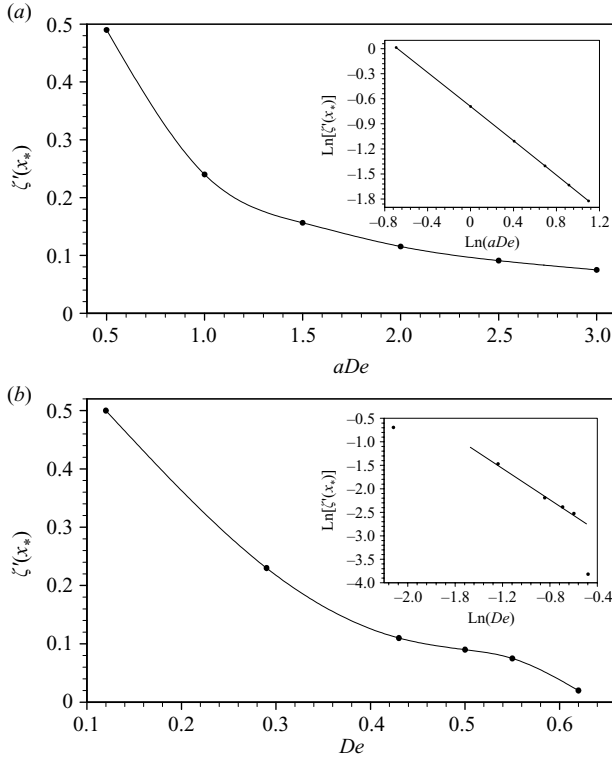
FIGURE 11. Influence of elasticity on the free-surface slope at x_*. Theoretical values are shown in (*a*) for $\varepsilon = 0.1$. Experimental values from Liang *et al.* (1999) are shown in (*b*). Insets depict the corresponding logarithmic values.

on dimensional arguments. The experimental values are shown in figure 10(*b*), which are estimated from figure 4 of Liang *et al.* (1999). The inset in the figure shows that x_* roughly increases with elasticity like De^4 for gravity-driven flow.

Another variable that is used for comparison between experiment and theory is the slope of the jet surface at x_* (see figure 8). Figure 11 shows the dependence of $\zeta'(x_*)$ on De based on the current theory (figure 11*a*) and the measurements (figure 11*b*) of Liang *et al.* (1999). Both the experimental and theoretical values indicate that the slope decreases with elasticity. The theoretical slope values in figure 11(*a*) are determined from (5.21) and (6.4), leading to

$$\zeta'(x_*) = \frac{c}{3}\varepsilon x_*^{-2/3} + \frac{1}{6}\varepsilon^2 \left(2B_3 x_*^{-1/3} - C_3 x_*^{-4/3}\right) \simeq \frac{0.52}{aDe} + \frac{0.70}{\sqrt{aDe}}\varepsilon^{3/2}. \qquad (6.13)$$

Thus, to leading order in ε, $\zeta'(x_*) \sim (aDe)^{-1}$, which, interestingly, is independent of the Reynolds number. The correction resulting from the addition of higher-order terms leads to a slightly different behaviour, namely $\zeta'(x_*) \sim (aDe)^{-1.03}$ based on the inset of figure 11(*a*). Experimental slope values from figure 4 of Liang *et al.* (1999) are reported here in figure 11(*b*) for comparison. Both theory and experiment indicate a downward trend of the slope, $\zeta'(x_*)$, with De, reflecting the flattening of the jet profile with increasing normal stress effect (see also figure 8). Figure 11 shows that in the middle range of Deborah numbers, the experimental trend, with $\zeta'(x_*) \sim De^{-1.8}$, is similar to the theoretical trend. However, there are some notable

qualitative differences between theory and experiment for the low- and high-*De* ranges. In contrast to theory, there is no definite trend for small or large *De*. The results of Liang *et al.* (1999) in figure 11(*b*) suggest a strong decrease of $\zeta'(x_*)$ towards zero for large *De*, in comparison to the smoother (asymptotic) decay exhibited by the current numerical values in figure 11(*a*). This suggests, perhaps, that the transition from necking to swelling, as *De* increases (*De* > 0.73 in figure 4 of Liang *et al.* 1999) occurs more suddenly for gravity-driven flow compared to inertia-driven flow. However, this cannot be confirmed by the present theory, which is based on moderately low Deborah number.

In sum, there is good qualitative agreement between the experimental trends observed by Liang *et al.* (1999) and the current theoretical predictions. One cannot expect good quantitative agreement for several reasons. While planar jet flow is considered in the current theory, axisymmetric jet flow was examined by Liang *et al.* (1999). The experimental jet flow is gravity driven, whereas the current flow is pressure driven. Another aspect that can lead to discrepancy between theory and experiment is the detachment of the fluid at the pipe lip observed by Liang *et al.* (1999). Whether this phenomenon is real or not remains unclear. Fluid properties can be another source of discrepancy, such as multiple relaxation times versus single relaxation time used for the Oldroyd-B model and shear-dependent viscosity versus constant viscosity. Finally, the current theory is based on the balance between inertial, viscous and elastic effects, whereas the experiment focused primarily on the interplay between gravity and elasticity.

7. The composite flow

Following Van Dyke (1964), the composite expansion operator is defined by

$$C_n \equiv (E_n + H_n - E_n H_n). \tag{7.1}$$

This expression provides a uniform approximation to order ε^n over the whole width of the jet.

7.1. *Composite flow field*

For $n = m = 3$, the composite expansion for the stream function becomes

$$C_3 \psi = \varepsilon^2 [x^{2/3} f_2(\theta) - 2z^2 h_1] + \varepsilon^3 [x f_3(\theta) + g_3(\theta)$$
$$+ 2(z - z^2) h_2 + \psi_3(x, z) - 2x] + O(\varepsilon^4). \tag{7.2}$$

Although the value of h_2 is required if the stream function is to be evaluated to $O(\varepsilon^3)$, this accuracy is not indispensable when the flow and stress variables are determined. This is the case, for instance, for the following expressions for the streamwise and transverse velocity components:

$$C_2 u(x, z) = \varepsilon x^{1/3} f_2'(\theta) + \varepsilon^2 [x^{2/3} f_3'(\theta)$$
$$+ x^{-1/3} g_3'(\theta) - 2z(B_3 x^{2/3} + C_3 x^{-1/3})] + O(\varepsilon^3), \tag{7.3}$$

$$C_2 w(x, z) = \frac{\varepsilon^2}{3} x^{-1/3} [(\theta + c) f_2'(\theta) - 2 f_2(\theta)] + O(\varepsilon^3). \tag{7.4}$$

These expressions dictate how the velocity profile changes over the width of the jet up to the second order. Note that to this order, elasticity affects *u* but not *w*. This is also the case of the pressure, with non-zero contribution entering only to third order,
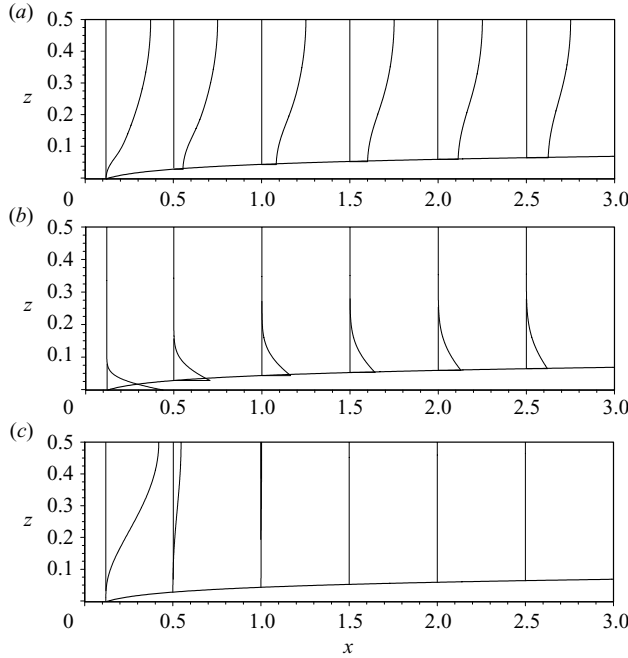
FIGURE 12. Dependence of (*a*) streamwise velocity, (*b*) transverse velocity and (*c*) pressure profiles on position for $aDe = 2$ and $\varepsilon = 0.1$.

namely

$$C_3 p(x, z) = \varepsilon^3 p_3(x, z) + O(\varepsilon^4), \tag{7.5}$$

where $p_3(x, z)$ is given by (4.20). The flow field (velocity and pressure) at different positions between the free surface and the centreline is shown in figure 12 for $\varepsilon = 0.1$ and $aDe = 2$. The u profiles in figure 12(*a*) indicate that to second order, Poiseuille flow is recovered at the centreline, so that $u(x, z = 1/2) = 0.5$. There is a strong deviation from the Poiseuille behaviour in the inner region and an overall flattening of the profile at large x. Figure 12(*b*) confirms that the transverse component of the flow is essentially absent except very close to the free surface. Simultaneously, the pressure profiles in figure 12(*c*) suggest the existence of strong pressure variation near the channel exit. Note, however, the small variation of pressure across the boundary layer (close to the free surface). The influence of elasticity, which is only reflected in the u profiles, is illustrated in figure 13 for $aDe \in [0, 3]$. The change in concavity inferred from figure 12(*a*) is now obvious. Elasticity appears to be mostly influential near the free surface. This will be confirmed next when the stress profiles are examined.

7.2. *Composite stress field*

In consistency with the order in the flow field, the composite expansions for the stress components are obtained to $O(\varepsilon)$. In this case,

$$C_1 q(x, z) = 2aDe\left(16z^2 + f_2''^2\right) + \varepsilon a\left\{\frac{1}{3}x^{-\frac{2}{3}}[f_2' - (\theta + c)\, f_2''\right.$$

$$\left. + 12De^2 f_2 f_2'' f_2''' + 12De f_2'' g_3''] + 4x^{1/3} De f_2'' f_3''\right\}, \tag{7.6}$$
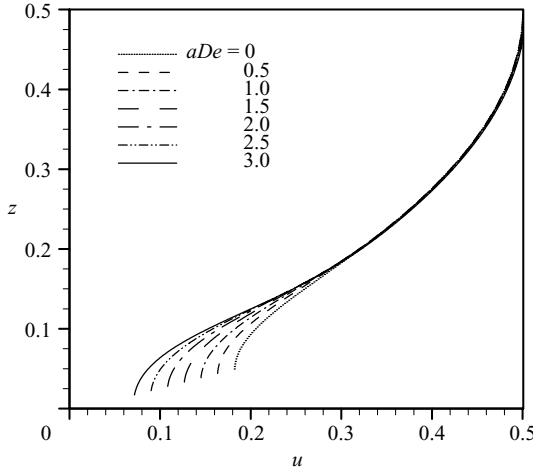
FIGURE 13. Influence of elasticity on the streamwise velocity profiles at $x = 0.5$ for $\varepsilon = 0.1$.

$$C_1 r(x, z) = \frac{2}{3} \varepsilon x^{-\frac{2}{3}} a [(\theta + c) f_2'' - f_2'] \tag{7.7}$$

and

$$C_1 s(x, z) = a f_2'' + \varepsilon a \left\{ x^{1/3} f_3'' + x^{-2/3} \left[g_3'' + \frac{2}{3} De(f_2 f_2''' - f_2' f_2'' + (\theta + c) f_2''^2) \right] \right\}. \tag{7.8}$$

The stress distribution across the flow is illustrated in figure 14 for $\varepsilon = 0.1$, $a = 0.25$ and $De = 8$, at the same x positions as in figure 12. Note in this case, $aDe = 2$ as for the profiles in figure 12. While r (figure 14b) decays monotonically with z, both q (figure 14a) and s (figure 14c) exhibit a maximum close to the free surface. Figure 14(b) suggests that the transverse normal stress component is strongest with a negative value at the free surface; its level decreases and reaches zero at a location that is higher as the free surface increases, mirroring the behaviour of w in figure 12(b). Similarly, figures 14(a) and 14(c) indicate that q and s tend to zero upon approaching the centreline, but only s vanishes at the free surface; refer to the dynamic conditions (3.7b) and (3.7c). Note that q does not vanish at the free surface but tends to a small value there. Overall, all stress components decay to zero rather rapidly with x. This behaviour is difficult to confirm directly from expressions (7.6)–(7.8), except perhaps for r. On the other hand, the behaviour near the centreline can be confirmed by taking the limit of the stress composite expressions for large θ. This is, again, easy to establish from (7.8); using (3.19), one observes that $C_1 r \to 0$ for large θ.

Expressions (7.6)–(7.8) clearly reflect the intricate difference in influence that elasticity and viscosity ratio can have on polymeric stress. Similar to p and w, the transverse normal stress component r depends only on viscosity ratio, as expression (7.7) suggests. This means that the traction normal to the flow at any position is uninfluenced by elasticity. In contrast, (7.8) indicates that s exhibits a linear dependence on De, whereas (7.6) shows that q varies quadratically with De. This dependence is confirmed in figure 15 in which q, r and s are plotted for $\varepsilon = 0.1$ and $a = 0.25$ for the range $De \in [0, 8]$, in figures 15(a)–15(c), respectively. Note that the apparent dependence of r on elasticity in figure 15(b) is only because of the shift of the free-surface level with De (see figure 8); otherwise the r profiles are similar. The influence of elasticity on q and s is best inferred by examining the strength of the
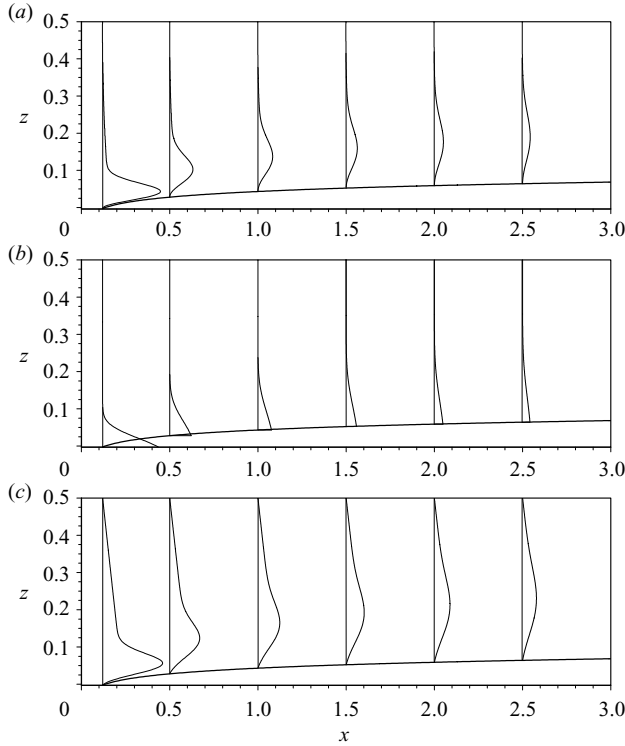
FIGURE 14. Dependence of (*a*) polymeric streamwise normal stress, (*b*) transverse normal stress and (*c*) shear stress profiles on position for $a = 0.25$, $De = 8$ and $\varepsilon = 0.1$.

maximum in figures 15(*a*) and 15(*c*). Note that a maximum (or minimum) must exist for s, since s vanishes both at the free surface and at the centreline. The maximum value, q_{max}, for q, for instance, can be estimated by inspecting (2.11*a*).

Thus, consider (2.11*a*) near the free surface. In this case, both s (see figure 14*c*) and w_z (see figure 12*b*) are weak. Moreover, at a distance relatively far downstream from the channel exit, q does not change significantly with x (see figure 14*a*). Under these conditions and noting that $w_z < 0$, (2.11*a*) leads to

$$q_{\max} \approx \frac{2a|w_z|}{1 - 2De|w_z|}, \tag{7.9}$$

which suggests that q_{max} grows with De. Recall that w_z is independent of De. The rate of growth of the q_{max} with elasticity is commensurate with that displayed in figure 15(*a*).

7.3. *Conservation of momentum flux and validation*

Finally, a valuable check on the current matching procedure can be carried out by examining the conservation of the momentum flux between the channel region far upstream and any position, $x = X$, outside the channel. The momentum integral is determined for the viscoelastic jet similar to Tillett (1968), which shows that the momentum flux is indeed conserved to $O(\varepsilon^3)$, which is the order of interest here. Thus, consider the momentum integral (4.23) along path (iv) in figure 6; note that
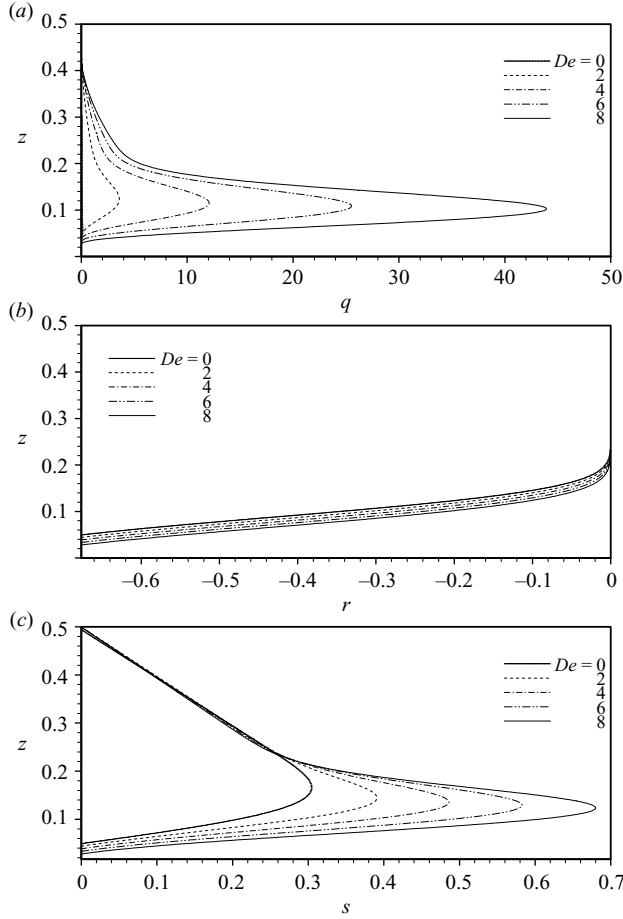
FIGURE 15. Dependence of (*a*) polymeric streamwise normal stress, (*b*) transverse normal stress and (*c*) shear stress profiles on elasticity at $x = 0.5$ for $a = 0.25$ and $\varepsilon = 0.1$.

$x_2 = X$ and is finite. The integral reduces to

$$M(X) = \int_{\zeta}^{1/2} \left[(p - 2\varepsilon^3 \psi_{xz} + \varepsilon^3 q) + \psi_z^2 \right]_{x=X} \mathrm{d}z. \tag{7.10}$$

The above integral can be expanded as

$$M = M_0 + \varepsilon^3 M_3 + o(\varepsilon^3). \tag{7.11}$$

Using (3.8) and (4.1*a*) to calculate ψ_z^2 in both the inner and outer regions and applying rule (7.1), one obtains the composite expression

$$C_3 \psi_z^2 = 4(z - z^2)^2 + \varepsilon^2 x^{2/3} \left[f_2'^2 - 4(\theta + c)^2 \right] + 2\varepsilon^3 [2(z - z^2)\psi_{3z}$$
$$+ x f_2' f_3' + f_2' g_3' + 4x(\theta + c)^3 - 2(B_3 x + C_3)(\theta + c)] + O(\varepsilon^4). \tag{7.12}$$

Substituting expressions (7.2), (7.5), (7.6) and (7.12) into (7.10) and using expression (7.11), one obtains

$$M_0 = \int_0^{1/2} 4(z - z^2)^2 \, \mathrm{d}z = \frac{1}{15} \tag{7.13}$$

and

$$M_3 = -\int_0^{cx^{1/3}} 4z^2\, \mathrm{d}z + \int_0^{1/2} [p_3 + 4(z - z^2)\psi_{3z}]\, \mathrm{d}z + \int_0^{1/2} q_0\, \mathrm{d}z$$

$$+ x \int_0^{\infty} \left[f_2'^2 - 4(\theta + c)^2 \right] \mathrm{d}\theta. \quad (7.14)$$

The first term in (7.14) is to account for the fact that the integration starts at $z = \zeta(x)$ and not $z = 0$ (see expression (7.13)). It is not difficult to see that the integration between 0 and $z = \zeta(x)$ gives higher-order terms which are negligible. The last term in (7.14) is a contribution from expression (7.12) and is simply obtained by changing the integration variable to θ. The first and the third terms in (7.12) can be integrated at once to give $-(4/3)c^3 x$ and $-(4/3)a\,De$, respectively; whereas for the last term, (3.17), (3.18a) and (3.19) are used to give $(2 + (4/3)c^3)x$. To calculate the second integral, $\psi_3(x > 0, z)$ is first determined by integrating expression (4.17) with respect to x and matching it with the integral of expression (4.8) at $x = 0$. In this case, one has

$$\psi_3(x > 0, z) = 2x V_0(z) + \sum_{n=1}^{\infty} \frac{A_n}{B_n} \mathrm{e}^{-\beta_n x} V_n(z). \quad (7.15)$$

Thus, upon using expressions (4.20) and (7.15), the second integral in (7.14) becomes

$$\int_0^{1/2} [p_3 + 4(z - z^2)\psi_{3z}]\, \mathrm{d}z = 8x \int_0^{1/2} (z - z^2) V_0'(z) = -2x, \quad (7.16)$$

where (4.9) and (4.18) are used. Thus, $M_3 = -(4/3)a\,De$ and $M = (1/15) - (4/3)\varepsilon^3 a\,De + o(\varepsilon^3)$. This proves that the momentum flux is indeed the same at any position (see §4.4).

8. Concluding remarks

Two-dimensional jet flow of a viscoelastic liquid emerging into the atmosphere is examined in this study. The Oldroyd-B constitutive model is adopted. The problem is of direct relevance to polymeric processes such as high-speed extrusion in which inertia plays a significant role. The effect of elasticity on the profiles of velocity and stress components and the interplay between fluid elasticity and inertia are investigated. Inertia is assumed to be large enough, allowing asymptotic development in terms of the inverse Reynolds number. In this case, the equations of motion and stress are reduced by expanding the flow field and the stress about the basic Poiseuille flow. A classical boundary-layer analysis is applied to find the flow adjacent to the free surface at which a boundary layer forms for moderate distances downstream from the channel exit. The influence of this boundary layer is investigated using the method of matched asymptotic expansions.

It is found that elastic or normal stress effects are most significant close to the channel exit. Interestingly, the viscosity ratio, a, and the Deborah number, De, do not appear separately in the case of flow field variables and free-surface expression but rather appear as the group aDe. Given the presence of relatively high inertia, the jet exhibits contraction for any Deborah number. However, elasticity tends to delay the contraction further downstream from the channel exit. The straight portion of the free surface of length x_* in turn reflects the balance between inertial and elastic effects very close to the channel exit. The length of the flat portion increases with elasticity. Moreover, normal stress effect weakens the contraction of the jet. A downward trend

of the slope of the free surface (at $x = x_*$) with elasticity is observed, reflecting again the flattening effect of the jet profile with increasing normal stress. Comparison of the transition length, x_*, and the free-surface slope at that position with measurements based on gravity-driven flow (Liang *et al.* 1999) leads to good qualitative agreement between the current theory and experiment. Closer or quantitative agreement is not expected despite the similarity between pressure-driven and gravity-driven flows. Numerical prediction of the boundary-layer thickness near the channel exit confirms the $\varepsilon^{3/2}\sqrt{aDe}$ behaviour based on dimensional arguments.

In general, elastic effects appear to be mostly influential near the free surface at which inertial effects are less dominant compared to the core region. The polymeric shear stress, s, exhibits linear dependence on De, whereas the streamwise normal stress component, q, varies quadratically with De; both have a maximum close to the free surface. The transverse normal stress component, r, is strongest at the free surface with a negative value and monotonically decreases to zero with height. All the stress components decay rapidly with x outside the channel.

Inspection of the flow at the centreline reveals that Poiseuille conditions for velocity and pressure are reached inside the channel at a distance about half the width of the channel, whereas the primary normal stress difference relaxes to the Poiseuille level at a distance about one width of the channel further upstream from the channel exit. A sharp gain in primary normal stress difference is predicted as the flow traverses the channel exit. A saturation effect of elasticity is observed for large De, suggesting that the stress relaxes to the Newtonian level at a relatively short distance downstream from the channel exit. The pressure relaxes to zero level at a distance about one width of channel downstream from the channel exit, whereas the streamwise velocity decreases linearly with x outside the channel, suggesting the overall flattening of the velocity profile. A momentum balance between the flow far upstream and far downstream of the channel exit reveals that the asymptotic contraction ratio of the viscoelastic jet decreases with elasticity of the fluid. This turns out to be in reasonable agreement with the results obtained close to the channel exit.

The scalings chosen are such that the jet Reynolds number is small and its Deborah number is of order one. One might expect therefore that viscoelastic effects would appear at the same order as viscous effects. However, because this is a shear-dominated flow in the surface boundary layer, viscous effects come in first, meaning that viscoelastic effects are secondary perturbations. This is of course helpful and rather essential to the present analysis, at the risk of excluding the case of more common interest in which the dominant balance is between elasticity and inertia.

In this regard, although most polymer processing applications occur essentially in the absence of inertia, the current work is useful for high-speed processes, for instance for fibre spinning (Donnelly & Weinberger 1975) and film casting (German & Khayat 2008). More importantly, the fundamental significance of the current work cannot be overstated. The matched asymptotic formulation clearly illustrates how the stress or velocity gradient singularity at the channel exit can be effectively dealt with. Despite the advent of powerful computational methodologies, the presence of this singularity remains a major obstacle in any numerical scheme. Mesh refinement, for instance, is one of the common tools used to achieve accuracy near the singularity. Pasquali & Scriven (2002) examined the influence of mesh density on the singularity for coating flow by interpolating the velocity gradient along the wall. They found that the components of the velocity gradient display large overshoots and undershoots in the proximity of the contact line, which become more pronounced as the mesh is refined. More importantly, they state that 'the large, rapidly varying components of

the velocity gradient affect strongly the computation of the polymer conformation near and at the contact line, severely limiting the maximum Weissenberg number at which a physically meaningful solution can be computed'.

The current asymptotic technique circumvents this problem altogether, as a similarity solution is available, which need not recognize the presence of the singularity, similar to boundary-layer flow near the edge of a plate. The current high-Reynolds-number flow naturally lends itself to similarity solution near the free surface, with elastic effects entering as higher-order terms. The existence of a similarity solution is essential. For highly elastic fluids, one can similarly seek an asymptotic solution assuming the elasticity or Deborah number is large. In this case, however, a similarity solution may or may not exist in the inner region, depending on the constitutive model. Although one can easily adopt a spectral expansion (see Khayat & Kim, 2006 and the references therein), the requirement of a boundary condition at some x remains problematic, precluding the main advantage of the similarity solution. On the other hand, a similarity solution is readily available for non-elastic shear-thinning and shear-thickening fluids (Zhao & Khayat 2007) and possibly for second-order fluids. For the upper-convected Maxwell model, which is closely related to the Oldroyd-B model used in the current formulation, a similarity does exist (Renardy 1997).

Finally, the current work is restricted to steady flow, and it is not at all obvious how it can be extended to transient flow. The presence of elasticity is known to cause flow instability, of oscillatory nature at large Deborah number. The interplay between inertia and normal stress is also expected to be destabilizing. In this regard, the current study constitutes an essential phase towards a full linear stability analysis, as it provides the steady-state flow, the stability of which is to be analysed.

REFERENCES

BÉRDAUDO, C., FORTIN, A., COUPEZ, T., DEMAY, Y., VERGNES, B. & AGASSANT, J. F. 1998 A finite element method for computing the flow of multi-mode viscoelastic fluids: comparison with experiments. *J. Non-Newton. Fluid Mech.* **75**, 1.

BIRD, R. B., ARMSTRONG, R. C. & HASSANGER, O. 1987 *Dynamics of Polymeric Liquids*, vol. 1, 2nd edn. John Wiley.

CAO, F., KHAYAT, R. E. & PUSKAS, J. E. 2005 Effect of inertia and gravity on the draw resonance in high-speed film casting of Newtonian fluids. *Intl J. Solids Struct.* **42**, 5734.

CLOITRE, M., HALL, T., MATA, C. & JOSEPH, D. D. 1998 Delayed-die swell and sedimentation of elongated particles in wormlike micellar solutions. *J. Non-Newton. Fluid Mech.* **79**, 157.

DONNELLY, G. J. & WEINBERGER, C. B. 1975 Stability of isothermal fibre spinning of a Newtonian fluid. *Ind. Engng Chem. Fund.* **14**, 334.

DOUFAS, A. K. & MCHUGH, A. J. 2001 Simulation of melt spinning including flow-induced crystallization. Part III. Quantitative comparison with PET spinline data. *J. Rheol.* **45**, 403.

EGGLETON, C. D., FERZIGER, J. H. & PULLIAM, T. H. 1994 Moderate Reynolds number entry flow and boundary layer approximations for a viscoelastic fluid. *Phys. Fluids.* **6** (2), 700.

GERMAN, R. & KHAYAT, R. E. 2008 Interplay between inertia and elasticity in film casting. *ASME J. Fluids Engng* **130**, 081501-1.

GOLDIN, M., YERUSHALMI, J., PFEFFER, R. & SHINNAR, R. 1969 Breakup of a laminar capillary jet of a viscoelastic fluid. *J. Fluid Mech.* **38** (4), 689.

KHAYAT, R. E. & KIM, K. 2006 Thin-film flow of a viscoelastic fluid on an axisymmetric substrate of arbitrary shape. *J. Fluid Mech.* **552**, 37.

LIANG, Y., OZTEKIN, A. & NETI, S. 1999 Dynamics of viscoelastic jets of polymeric liquid extrudate. *J. Non-Newton. Fluid Mech.* **81**, 105.

MIDDLEMAN, S. & GAVIS, J. 1961 Expansion and contraction of capillary jets of viscoelastic liquids. *Phys. Fluids.* **4** (8), 963.

MIYAKE, Y., MUKAI, E. & IEMOTO, Y. 1979 On a two-dimensional laminar liquid jet. *Bull. Jpn Soc. Mech Engng* **22** (72), 1382.

OLDROYD, J. G. 1950 On the formulation of rheological equations of state. *Proc. R. Soc. Lond.* A. **200**, 523.

PASQUALI, M. & SCRIVEN, L. E. 2002 Free surface flows of polymer solutions with models based on the conformation tensor. *J. Non-Newton. Fluid Mech.* **108**, 363.

PHILIPPE, C. & DUMARGUE, P. 1991 Étude de l' établissement d'un jet liquide laminaire émergeant d'une conduite cylindrique verticale semi-infinie et soumis à l'influence de la gravité. *J. Appl. Math. Phys.* (*ZAMP*) **42**, 227.

RENARDY, M. 1997 High Weissenberg number boundary layers for the upper convected Maxwell fluid. *J. Non-Newton. Fluid Mech.* **68**, 125.

RENARDY, M. 2002 Similarity solutions for jet breakup for various models of viscoelastic fluids. *J. Non-Newton. Fluid Mech.* **104**, 65.

ROTEM, Z. 1964 Axisymmetrical free laminar jet of incompressible pseudo-plastic fluid. *Appl. Sci. Res.* **13** (A), 353.

SCHUMMER, P. & THELEN, H. G. 1988 Break-up of a viscoelastic liquid jet. *Rheol. Acta.* **27**, 39.

SEYFZADEH, B., HARRISON, G. M. & CARLSON, C. D. 2005 Experimental studies on the development of a cast film. *Polym. Engng Sci.* **45**, 443.

SHAH, Y. T. & PEARSON, J. R. A. 1972 On the stability of nonisothermal fibre spinning-general case. *Ind. Engng Chem. Fund.* **11**, 150.

SHI, J. M., BREUER, M. & DURST, F. 2004 A combined analytical–numerical method for treating corner singularities in viscous flow predictions. *Intl J. Num. Methods Fluid.* **45**, 659.

SLATTERY, J. C. & LEE, S. 2000 Analysis of melt spinning. *J. Non-Newton. Fluid Mech.* **89**, 273.

STEHR, H. & SCHNEIDER, W. 1996 Submerged jet flows of non-Newtonian fluids. *Appl. Math. Mech.* (*ZAMM*) **76**, 497.

TANNER, R. I. 1999 *Engineering Rheology*. Oxford University Press.

TIEU, H. A. & JOSEPH, D. D. 1983 Extrudate swell for a round jet with large surface tension. *J. Non-Newton. Fluid Mech.* **13**, 203.

TILLETT, J. P. K. 1968 On the laminar flow in a free jet of liquid at high Reynolds numbers. *J. Fluid Mech.* **32**, 273.

TOME, M. F., MANGIAVACCHI, N., CUMINATO, J. A., CASTELO, A. & MCKEE, S. 2002 A numerical technique for solving unsteady viscoelastic free surface flows. *J. Non-Newton. Fluid Mech.* **106**, 61.

TRAN-CONG, T. & PHAN-THIEN, N. 1988 Three-dimensional study of extrusion processes by boundary-element method. II. Extrusion of a viscoelastic fluid. *Rheol. Acta.* **27**, 639.

VAN DYKE, M. D. 1964 *Perturbation Methods in Fluid Mechanics*. Academic Press.

WILSON, D. E. 1985 A similarity solution for axisymmetric viscous-gravity jet. *Phys. Fluids.* **29** (3), 632.

ZHAO, J. & KHAYAT, R. E. 2007 Spread of non-Newtonian liquid jet over a horizontal plate. *J. Fluid Mech.* **613**, 411.